DEVELOPMENT OF A HIGH LOAD CAPACITY TEST RIG TO EVALUATE THE STATIC PERFORMANCE OF PROCESS FLUID LUBRICATED THRUST BEARINGS

A Thesis

by

ZHENG BIAN

Submitted to the Office of Graduate and Professional Studies of
Texas A&M University
in partial fulfillment of the requirements for the degree of

MASTER OF SCIENCE

Chair of Committee,	Adolfo Delgado-Marquez
Co-Chair of Committee,	Luis San Andrés
Committee Member,	Chao Ma
Head of Department,	Andreas A. Polycarpou

May 2019

Major Subject: Mechanical Engineering

ABSTRACT

Electrical submersible pumps (ESPs) are artificial lift devices widely used in the oil and gas industry to increase production. For unconventional wells, which includes subsea applications, installation cost is an order of magnitude higher that the cost of the typical ESP, thus pump reliability is paramount. Contamination of the thrust bearing lubricant oil by process fluid due to seal failures is one of the leading causes of thrust bearing failure. While improving seal reliability can prevent thrust bearing failures, an alternative approach is to develop process-fluid lubricated thrust bearings.

This research aims to characterize and study the performance of thrust bearings operating with process fluid lubrication. A component level-level test rig for testing the performance of thrust bearings in any mixture of water, sand, and air is designed, built, and commissioned. Initial tests of the PEEK and Tungsten Carbide (WC) bearings include a load capacity test to determine the hydrodynamic limit of the bearing, a hydrodynamic test to corroborate test rig stability, and a wear test to determine if the bearings can operate feasibly past hydrodynamic limits in a mixed lubrication regime. Initial results show that lubrication starvation can occur in an unpressurized chamber for low viscosity fluids that are not supplied directly to the bearing. Furthermore, the film thickness, temperature rise in the pads, and load capacity all are lower for water lubricated bearings when compared to oil lubricated bearings. Results suggest that liner material affects wear rate but not load capacity; however, operating even the WC bearings past hydrodynamic limits causes substantial wear and is not recommended as an operating mode. Future work should focus on testing with sand and air as well as modifying the lubricant supply line to feed directly to the bearing.

ACKNOWLEDGEMENTS

I would like to thank Dr. Adolfo Delgado for his continual guidance throughout my graduate years as well as Dr. Abhay Patil for his frequent expertise and advice. I could not have done this project without their continued support. I would like to thank Dr. San Andres for his insightful comments and suggestions during commissioning phase of the test rig. Furthermore, I am grateful to Hector Casillas and Shell as they made this project possible.

I would also like to extend my gratitude to three students who helped me greatly with this project: Harley May who helped design the test structure, Rasool Koosha who helped run XLTRC simulations and provided simulation data, and Sean McClean who provided assistance during commissioning.

Last but not least, I would like to acknowledge the support of my parents, Hongyu and Kejian. They have provided immeasurable support and I am forever grateful.

CONTRIBUTORS AND FUNDING SOURCES

The principal investigator for this work is Professor Adolfo Delgado-Marquez in collaboration with Dr. Abhay Patil of the Texas A&M Turbomachinery Laboratory. The thesis committee members include Professor Adolfo Delgado-Marquez and Professor Luis San Andrés from the Department of Mechanical Engineering and Professor Chao Ma from the department of Manufacturing and Mechanical Engineering Technology.

Funding is provided through a partnership with Shell Oil Company.

NOMENCLATURE

HSUS	Humane Society of the United States
ESP	Electrical Submersible Pump
PEEK	Polyetheretherketone Thermoplastic
SiN	Silicon Nitride
WC	Tungsten Carbide
ATSP	Aromatic Thermosetting coPolyester Composite
B/L	Wide Long Ratio (radial width over intermediate diameter)
PFA	Polyperfluoroalkoxyethylene
OD	Outer Diameter
ID	Inner Diameter
OEM	Original Equipment Manufacturer
DE	Drive End
NDE	Non Drive End
HP	Horse Power

TABLE OF CONTENTS

Page

LIST OF FIGURES

Page

LIST OF TABLES

Page

1. INTRODUCTION

During the production life cycle of an oil well, the bottomhole pressure may drop low enough to require artificial lift mechanisms to boost oil production. Among the artificial lift mechanisms available, the Electrical Submersible Pumps (ESPs) are a common selection due to their ability to move large fluid volumes [1]. An ESP is a vertical multistage centrifugal pump consisting of a pump, a seal, and a motor. The pumped fluid typically consists of hydrocarbons, water, and sand from the reservoir or introduced through fracking.

The installation of ESPs in deep water applications is extremely expensive. The cost of replacing a failed ESP in such scenarios can be more than the ESP unit itself [2]. One of the primary failure mechanisms of an ESP is a failure of the seals from excessive vibrations [3]. This causes process fluid to contaminate the thrust bearing lubricant and cause bearing seizure and ESP failure. Two approaches to address this failure mode include improving the seals or designing a process fluid-lubricated thrust bearing. This study focuses on the latter. The use of properly qualified process fluid lubricated thrust bearings can reduce maintenance costs and increase the longevity of ESPs downhole operation even when there is a seal failure.

2. LITERATURE REVIEW

This section reviews the existing literature pertaining to process fluid lubricated thrust bearings. The first section includes a brief background on tilting pad thrust bearings and their limitations for subsea applications, followed by a discussion on process fluid lubrication. The last section concentrates on suitable bearing materials and coatings for water lubrication, existing test rigs and their applicability to this study.

In typical ESP configurations, the oil in the motor that lubricates the thrust bearings are isolated from the process fluid via seals. Unfortunately, seals are one of the main modes of failure in an ESP. Once the seals fail, process fluid, which could include abrasives such as sand, can contaminate the lubricant and induce bearing failure via erosion or abrasion [4]. Process fluid in an ESP can be any combination of oil, water, sand, and gas. This project focus on water as a starting point for further studies.

The concept of water-in-oil lubricant contamination is often viewed as a negative issue in any rotating machinery that lubricates with one but processes the other; however, Harika [5] et al. examined the impact of water contamination in oil lubricants and found positive effects on load capacity when the emulsion is properly handled. Proper design and modeling of the hydrodynamic film can prevent cavitation of the fluid mixture while inhibitors can be added to prevent chemical reactions such as oxidation. Figure 1 shows experimental results demonstrating that an oil mixture with 10% water emulsion by mass exhibits higher film thickness, friction torque, and lower temperatures than the pure oil.

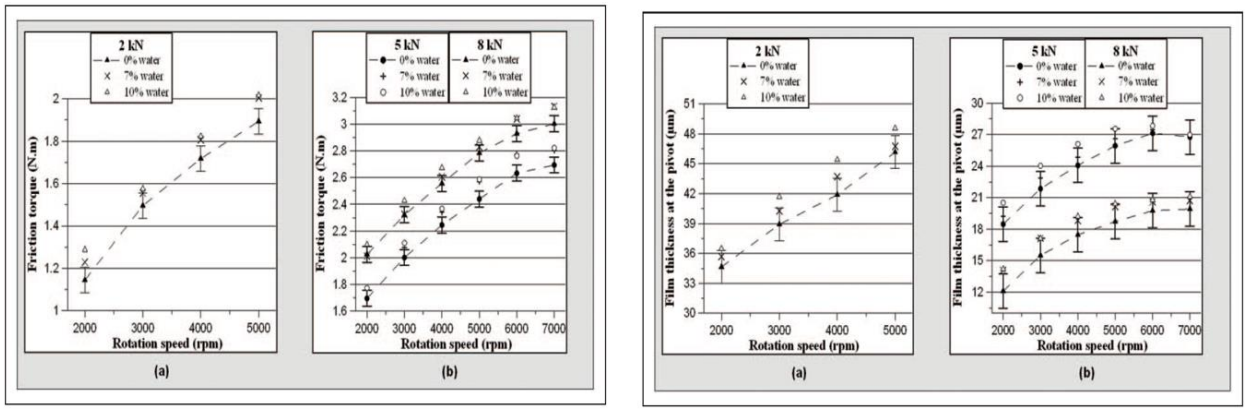

Figure 1 Friction torque and film thickness for 0%, 7%, and 10% water emulsion by weight [5]

The improved thermal performance of the lubricant is expected as water transfers heat better than oil. Harika [6] later conducted rheological experimental and numerical studies on water-oil emulsions and concluded that though the water-oil mixture exhibited slightly higher viscosity due to the flow resistivity of water droplets and film thickness, the most significant effect was a much lower pad operating temperature.

Zhang [7] et al. compiled a list of parameters to consider when designing a tilting pad bearing for water lubrication. One factor is the use of an adequate self-lubricating material. This helps the bearing and runner sustain less wear in start-up and boundary lubricating conditions, which are more prevalent due to the low viscosity of water. Higher viscosity and a width/length (B/L) ratio of 1 contributes to better performance, while minimizing surface roughness on the bearing face can reduce eccentric wear.

In terms of bearing structural parameters for fixed geometry bearings, Liu [8] et al. modeled numerically an elastic fixed slope pad using finite differences and found that both the inclination angle of the pad as well as B/L ratio greatly affects the performance of the bearing. An optimal inclination angle for film thickness exists at 0.01˚. As the B/L ratio increases, film

thickness decreases while fluid pressure and friction coefficient increase. Inoue and Deguchi [9] investigated PEEK coated water lubricated tilting pad thrust bearings and found that an offset pivot support provided more film thickness stability than a center pivot support for the given range of speed of 0 to 300 RPM.

When lubricating with water instead of oil, the lower viscosity will generate high Reynolds numbers and lead to turbulent flow; however, while turbulence is negative for oil lubrication, it can be potentially beneficial in water lubrication [10]. Deng et al. conducted a numerical study and found the minimum film thickness increased with turbulence and decreased with stronger inertial effects. Abramovitz [11] experimentally found an increase in friction torque once the Reynolds number passed a certain value deemed to be the boundary between laminar and turbulent flow.

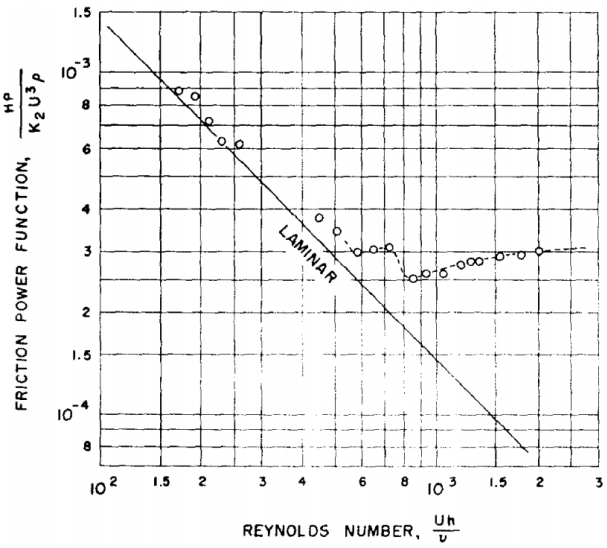

Figure 2 Friction torque vs Reynolds number for water lubrication showing the torque effects when transitioning from laminar to turbulent flow [11]

The process fluid for ESPs is often high temperature and laden with sand particles of various concentrations. These can have a negative abrasive impact on wear and friction [12]. Hu

et al. found that sand concentrations as small as 2% by weight can cause an increase in wear volume of up to 45%, and even a 100% increase in wear at high temperatures.

There are many different types of tilting pad materials and coatings including PTFE, PEEK, Tungsten Carbide (WC), and more. Coatings are often used to promote better lubrication compatibility, reduce wear, increase load capacity, increase tolerance against wear, or tune rotordynamic coefficients. Nie and Wang et al. [13] found that PTFE coated bearings develop less stiffness and damping than a conventional Babbitt coated pad but yield a very low coefficient of friction. Furthermore, experiments done by Mahieux [14] show that PTFE insulated the pad from higher temperatures, which reduced the tilt angle compared to Babbitt. PEEK, another common polymer in water lubrication, is often used instead of PTFE in today's application for water lubrication due to its better performance under load and high temperatures. Comparisons between PEEK and PTFE by Wodtke and Wasilczuk [15] show that PEEK deforms much less than PTFE at high temperatures and maintains a linear Young's modulus profile with increasing deflection (PTFE decays exponentially).

While polymer coatings are common, the bonding point between polymer and steel act as a failure point. Full polymer pads would appear to be a solution but are not typically deployed due to the permanent deformation caused by high Hertzian contact stresses when in operation. Despite these setbacks, Dieter, Thomas, and Lorenz [16] qualified a full PEEK bearing thrust pad by using an embedded steel pivot to circumvent Hertzian deformation and a modified PEEK composite with 50% carbon fiber content in its body. When tested with water as the lubricant at 75 psi (0.52 MPa) unit load, the bearings experienced no appreciable wear after 50 hours of continuous operation and 250 start-stop tests. PEEK was selected for its favorable chemical resistance as well as performance at high temperatures.

While polymer coatings may be softer than the traditional Babbitt, there are coatings that aim to increase the hardness of the bearing surface as well. In oil and gas, downhole drill string motors commonly use Polycrystalline Diamond (PCD) coated mixed lubrication thrust bearings. PCD bearings are selected over ball or roller bearings due to its ability to handle high loads and abrasive fluids with acceptable life [17]. PCD bearings undergo a run-in test for approximately 100 hours before they reach their optimal load capacity and friction coefficient. This process smooths out the diamond pad's surface roughness and allows the bearing to operate slightly in the hydrodynamic regime [18]. A PCD bearing with optimized geometry can even operate in full fluid film environment. For example, Sexton and Knuteson [19] showed that a PCD bearing with wedge shaped diamond inserts instead of circular inserts were able to enter full hydrodynamic lubrication in a 95/5 water glycol mixture with very low friction coefficient at speeds as low as 150 RPM or 0.5 m/s at 2000 psi (13.78 MPa) unit load after run-in. Russell [20] compared PCD performance against both ball bearings and modified tilting pad thrust bearings with spring loaded SiC coated pads. Russell found that the continuous runner profile of the tilting pad promoted a more stable pressure along the bearing face compared to the discontinuous runner of the PCD bearing pair. He concluded that hydrodynamic bearings with coated tilting pads are a more ideal solution for downhole motors facing abrasive fluids when compared to contact bearings due to less induced wear. His conclusion aimed to emphasize the use of fluid film bearings over mixed lubrication bearings.

An alternative to coating the pads is to redesign the bearing for water lubrication. Liang et al. [22] designed a water lubricated tilting pad bearing with rubber supports instead of pivot contacts. The benefit offered by the rubber include uniform load distribution and axial vibration

dissipation or axial damping. Unfortunately, rubber's properties are highly dependent on temperature and thus its use with ESP process fluid may be limited without further research.

A review of the existing literature on test rig construction for thrust bearings follows. Russell [20] created a robust yet simple test rig that allowed the testing of ball bearings, mixed lubrication PCD bearings, and hydrodynamic bearings at a variety of loads and speeds. The test rig is a vertical chamber flooded with lubricant and uses hydraulic cylinders to supply the load. The motor is mounted beneath the rig and slave bearing tilting pads handle the reaction load. The test rig, pictured in Figure 3, can provide thrust loads of up to 7000 lbs (31.1 kN) and speeds of up to 1000 RPM.

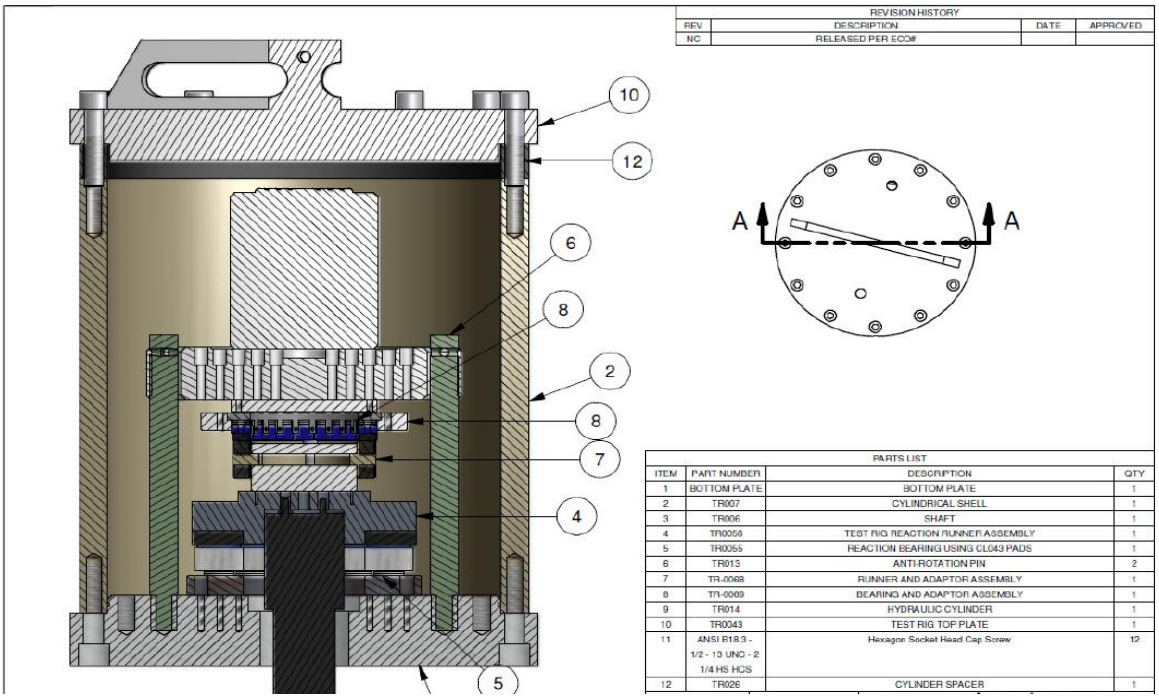

Figure 3 Russell's thrust bearing test rig cross section with labeled components [20]

Figure 4 depicts Harika's [6] water contamination test rig. A pneumatic jack delivers the force instead of a hydraulic system. The method of sealing or use of slave bearings is unclarified

but the rig is capable of 10,000 RPM and 8 kN (1798 lbs) of applied load. Pasanen's test rig, built with the intentent to test hydrodynamic thrust bearings, follows a similar design [23].

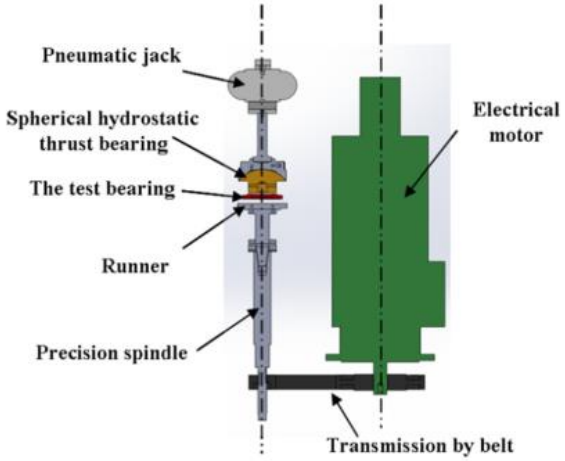

Figure 4 Harika's test rig schematic for water oil contamination with notable features captioned [6]

Gregory and Kingsbury developed a horizontally mounted test rig featuring a sliding housing for easy access to the test bearing [24]. The test rig was capable of large loads of 22,000 lbs (97.8 kN) and speeds of up to 11,000 RPM, but can only test one bearing at a time and uses clean oil lubricant.

The following section describes the current test rig design which incorporates a vertical chamber design with a hydraulic load system like Russell's test rig and disassembly chambers similar to the Kingsbury test rig.

3. EXPERIMENTAL FACILIITES

Figure 5 shows a partial cut view of the test rig design. The design borrows from the Russell [20] test rig by featuring a flooded lubrication chamber. However, a mechanical shaft seal isolates the slave bearings from the test bearing and the test fluid. The slave bearings are tapered roller bearings, grease lubricated. The rig design includes an oil mist injection hole in the spindle to implement active lubrication and enable high-speed operation (up to 3600 RPM) if needed for future testing. Three hydraulic cylinders, capable of 10 metric tons of force each, uniformly push the test bearing through thick plates against the thrust runner. The end plate easily detaches from the bottom for quick access to the bearing chamber following a similar set up as Kingsbury's rig [24]. A large removable spacer offers the option to test bearings in tandem. Slip-fit dowel pins keep the bottom assembly of end plate, spacer, cylinders, and loader plates stationary while the runner rotates freely with the rest of the spindle.

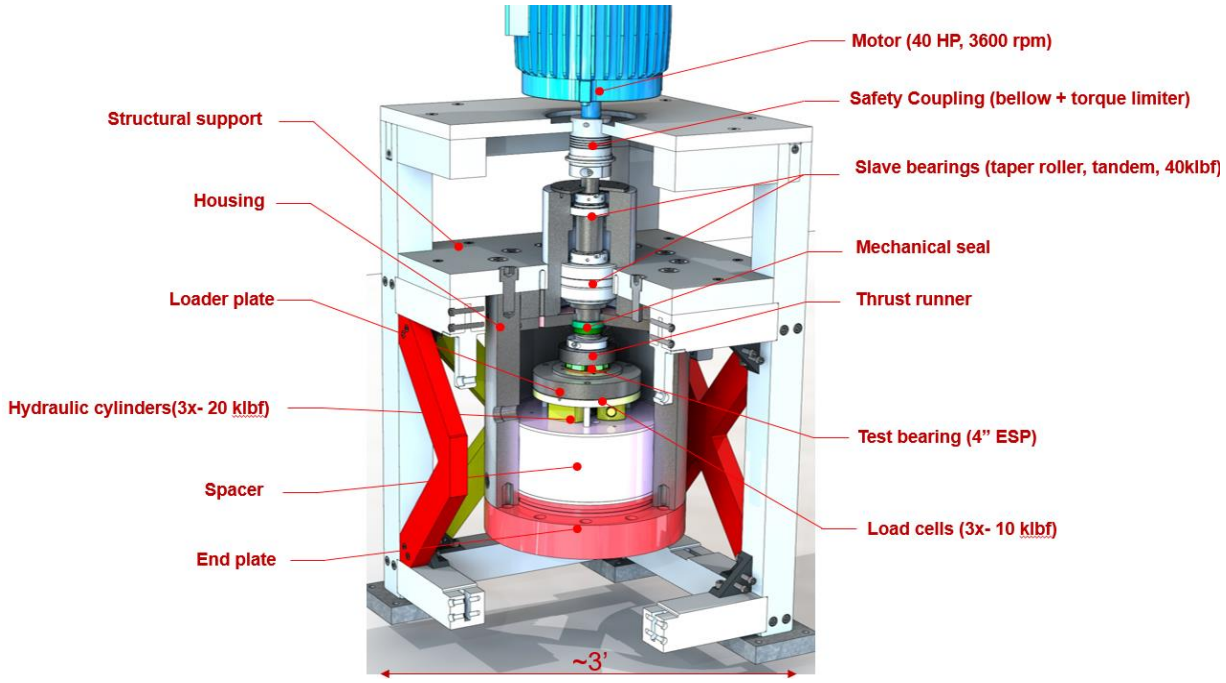

Figure 5 Proposed test rig schematic detailing main components

Figure 6 presents the schematic of the constructed test rig. Water circulates out of a reservoir through a heat exchanger to ensure steady temperatures before receiving fresh sand from a stepper-motor auger. The diaphragm pump, which operates with an accumulator, moves the slurry through a check valve and then promptly mixes with the injected air and enters the casing housing. The lubricant circulates out through the back of the test chamber and passes through a filter that collects the sand before reentering the reservoir.

The air flow starts by passing through a filter before diverting into two directions. One directs the air to the pump and accumulator. The other flow path directs the air across a mass flowmeter and an electronically controlled valve before mixing with the liquid lubricant. Pressure sensors and check valves monitor the inlet pressure and prevent backflow, respectively. The test rig instrumentation includes 3 load cells, 3 displacement probes, and 10 RTDs in the test chamber as well as a contactless torque transducer/tachometer dual sensor at the shaft driven end.

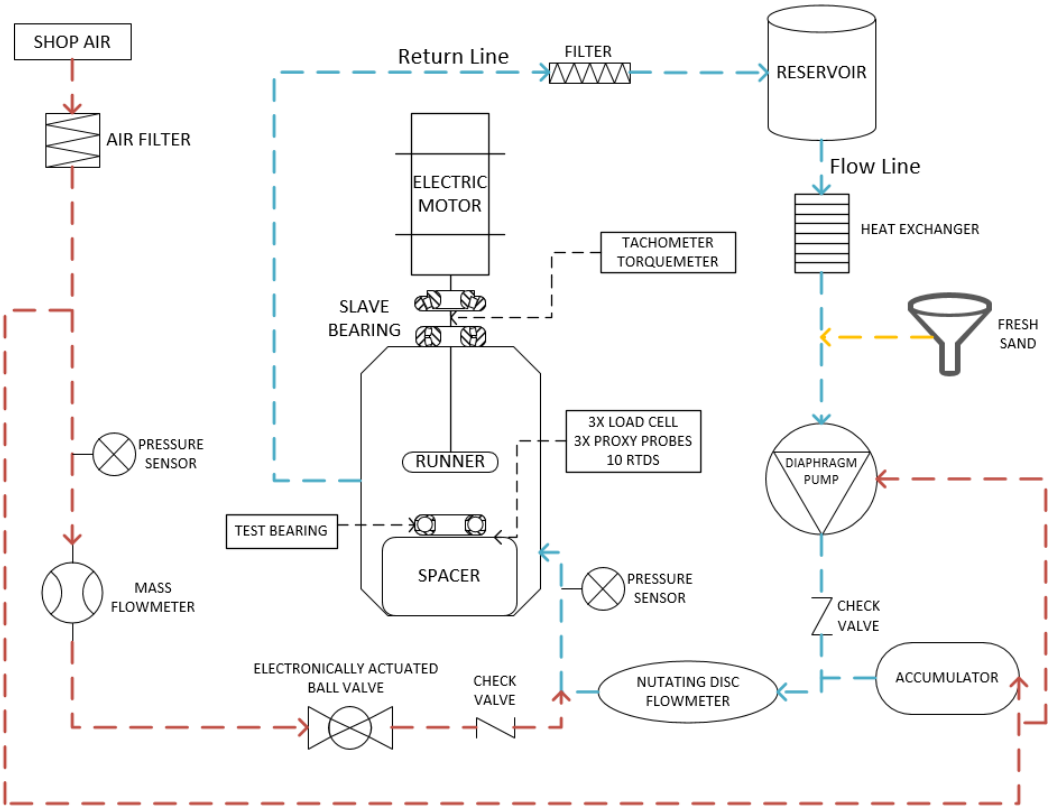

Figure 6 Proposed test rig diagram and floor plan

3.1 Test Rig Features

The component level thrust bearing test rig comprises of two main assemblies: the load driving assembly and the slave bearing spindle assembly. The load driving assembly is responsible for generating the axial load to the bearing and the slave bearing spindle assembly reacts the thrust load while driving the thrust collar at a constant speed. The design of these components aimed to satisfy the following functions:

- Test bearing accessibility: access the bearing with minimal removal of parts and without affecting motor alignment.
- Tests with water and sand: ability to test with variable amounts of air and sand.

- Reach high unit loads: the test rig must be able to apply high axial force to test bearings at high unit loads (>700 psi) without any damage or deformation to the rig setup.
- Test bearings to failure: ability to test bearings until seizure without damaging the test rig.
- Perform wear tests: able to hold a specific load for extended periods of time to conduct long term wear testing.
- Test two bearings in tandem: the rig must be able to accommodate two or more bearings in tandem.
- Multiple bearing sizes: the test rig must be able to accommodate any bearing size up to 8".

A detailed description of each assembly and critical component follows.

3.1.1 Load Driving Assembly

The load driving assembly, located at the bottom of the test rig, comprises of an end flange (red) attached to the housing, a spacer plate (pink), three hydraulic cylinders (yellow), a load cell plate (yellow), three load cells, and a bearing plate (grey). Figure 7 details the location of these items in the load driving assembly. A critical design feature of this assembly is to provide a uniform axial force driving the bearing into the runner. An external hand pump powers the low profile submersible hydraulic cylinders and an external pressure manifold distributes the pressure uniformly among the three cylinders. The load cell plate (yellow), mounted above the hydraulic cylinders, houses the load cells measuring the force applied to the bearing. The grey bearing plate distributes the point loads from the cylinders into a uniform axial load pushing the bearing onto the thrust runner.

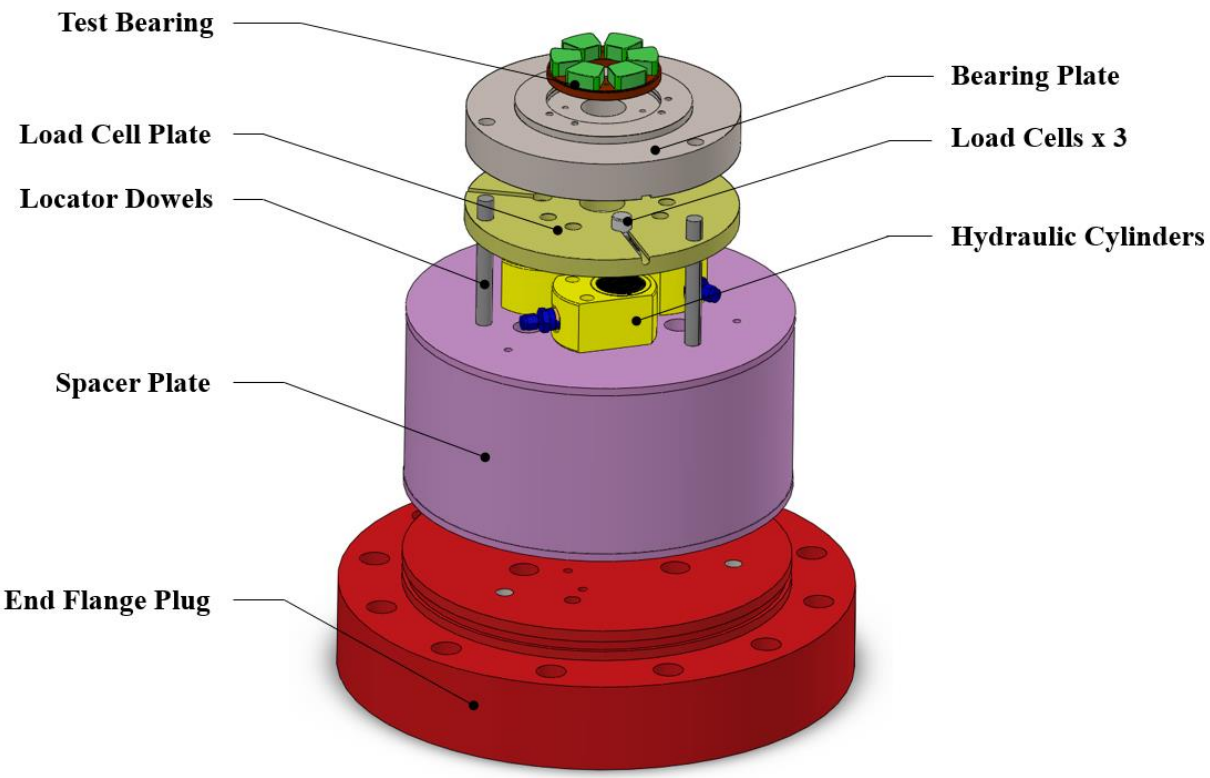

Figure 7 Load driving assembly model and notable components

The end flange (red) holds the components through twelve 1” bolt holes threaded to the 12” ID coated carbon steel chamber casing. A gland housing machined on of the pilot shoulder of the end flange houses a #381 O-ring to seal the bottom end of the chamber. The ID of the plug has a 0.001” diametric clearance with the ID of the casing to ensure good alignment when assembled. Three 3/8” holes drilled at the bottom of the plug provide a pathway for instrumentation inside of the test rig. Feedthroughs sealed holes while allowing routing the instrumentation cables through the bottom holes.

The spacer (pink) is a semi-hollow component that fills up space in the test chamber during single bearing testing. This additional space will allow for future tandem bearing testing. Using the spacer allows flexibility when switching from one test bearing to two without major

design modifications. The spacer also has through holes for instrumentation. The spacer's 12.05" ID features a 0.001" clearance respect to the ID of the test bearing casing, but includes an undercut through the middle portion to lighten the machining precision required while maintaining good alignment when assembling.

The hydraulic cylinders(yellow), each capable of 11.2 US tons of load, sit on top of the spacer (or plug if testing two bearings) following a symmetric orientation (120^{o} apart) in a slightly slanted fashion allowing them to fit inside the test chamber. The high-pressure tubing that replaces the OEM hose connections provide a smaller form factor, better fit inside of the test chamber, and better leakage sealing on the outside of the rig. An external hydraulic hand press connected to a pressure gauge distributes hydraulic fluid to the three cylinders through a pressure manifold. All equipment is rated for an operating pressure of 10,000 psi (68.94 MPa).

The load cell plate features three counterbores securing the load cells in place. The load cells are submersible and capable of reading 10,000 lbs (44.4 kN) of force each. The axial channels provide relief for the load cell wiring and three dowel through holes ensure both alignment and prevent rotation of the assembly.

The bearing plate (grey) houses the bearing and includes three dowel slots machined onto the counterbore to accommodate different bearing geometries and to prevent bearing rotation when testing. The plate thickness selection was determined from the results of a Finite Element Analysis (FEA) conducted to evaluate bending as the plate transfers the point loads from the hydraulic cylinders to the bearing uniformly. Three threaded through holes drilled next to the bearing secure the proximity probes measuring the relative distance of the runner to the bearing surface.

Figure 8 depicts the vertical test chamber housing load driving assembly. The test chamber casing is a coated carbon steel casing selected for its availability, lead time, and economic advantage over boring a solid stainless-steel round stock. The chamber includes threaded (UNF) bolt holes at the axial ends for assembly and radial holes (NPT) along its length for lubricant in/out ports. The inner diameters of the casing interfacing with other components (locational features) feature a dimensional tolerance of ~0.001" to ensure alignment of the multiple components upon assembly. In addition to the inlet and outlet holes for the lubricant bath, a relief channel machined on the top side of the top flange collects fluid that leaks through the seal.

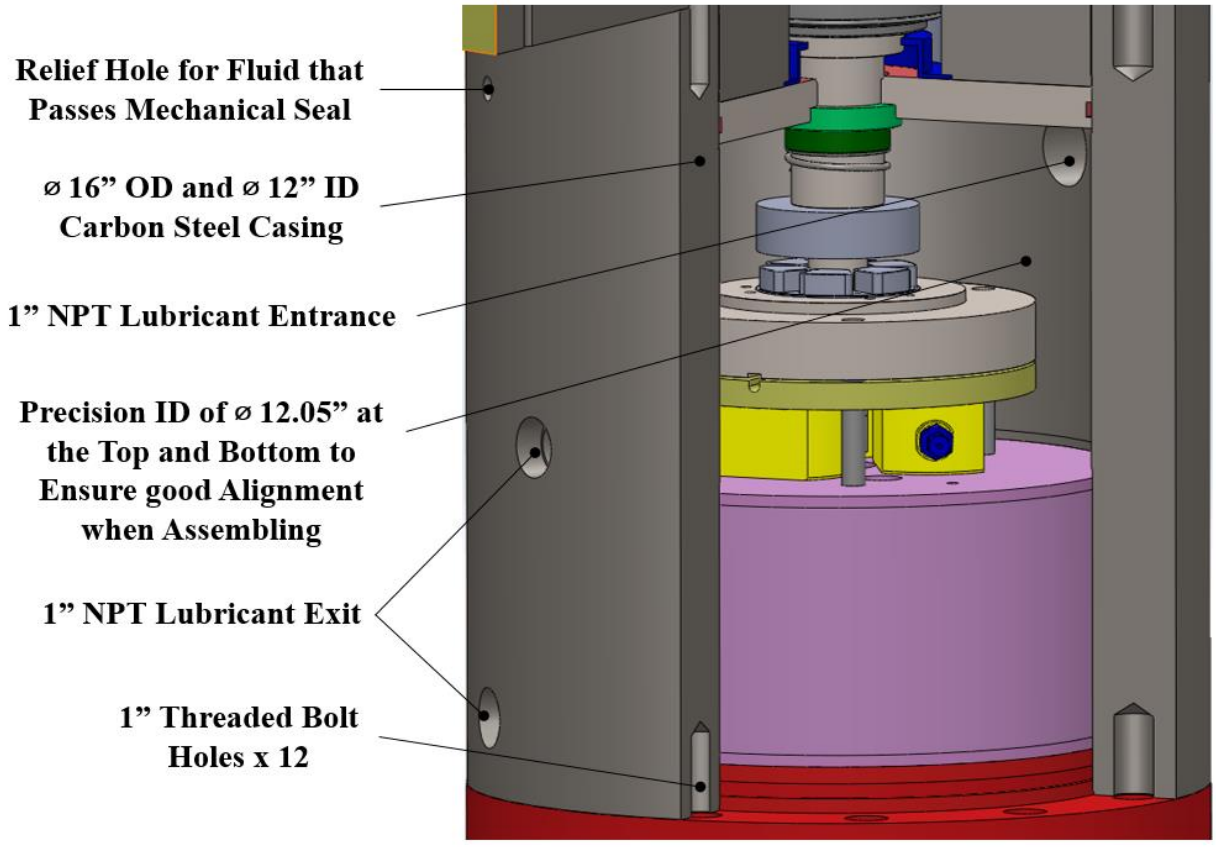

Figure 8 Test chamber casing model and notable features

3.1.2 Slave Bearing Spindle Assembly

Figure 9 depicts the slave bearing assembly featuring an isolation blind flange(red), slave bearing housing (grey), water protection sleeve (blue), mechanical shaft seal (green), two tapered roller slave bearings, shaft (shaft), and the thrust runner(grey). The purpose of the spindle assembly is to create a low maintenance system that can take the load generated by the hydraulic cylinders and maintain alignment between the shaft, motor, and casing. It also serves to isolate the test chamber from the slave bearing chamber. This is a critical feature for testing bearings lubricated with a of water, sand and gas mix.

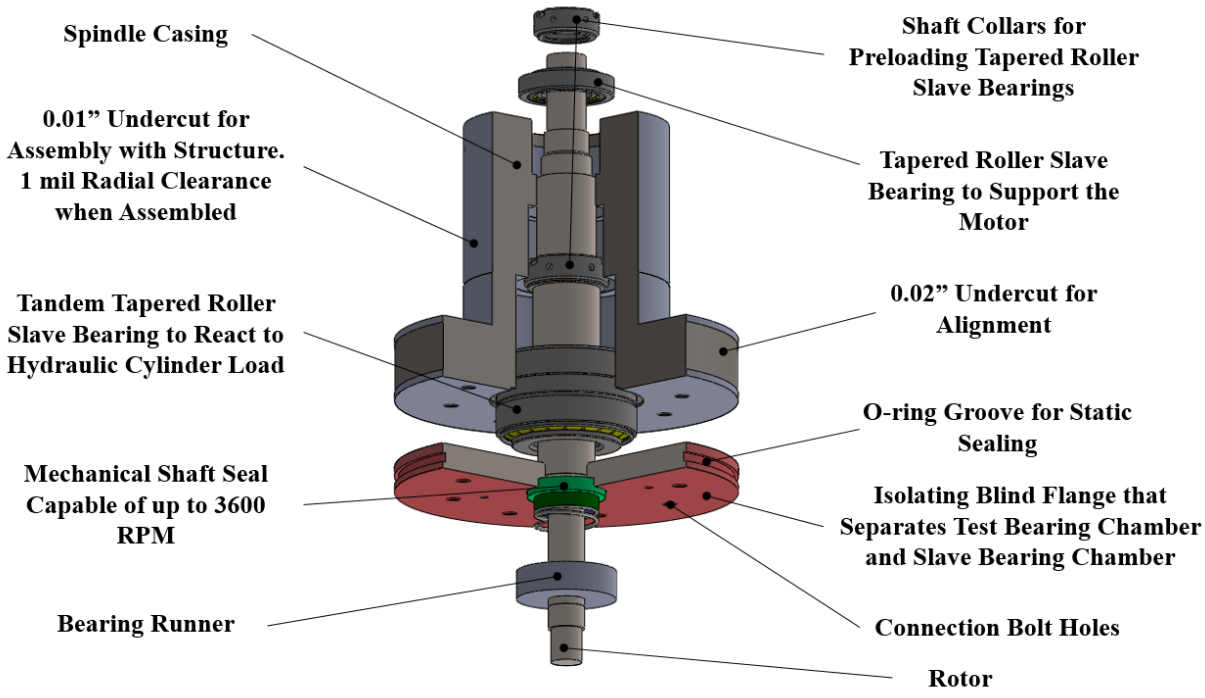

Figure 9 Slave bearing spindle assembly model and component descriptions

The spindle casing houses two tapered roller bearings that center the shaft and react to the axial load from the hydraulic cylinders and motor. The single tapered roller bearing near the drive end of the shaft serves as radial support while the tandem tapered roller on the opposite end

support both radial loads and axial loads from the hydraulic cylinders. Two threaded collars preload the slave bearings and an undercut on the OD provides two shoulders to align the spindle assembly respect to the test chamber. Figure 10 shows a partial cut-view of the spindle housing with the bearings installed. The end flange includes bolt holes that connect to both the isolating blind flange and the structure.

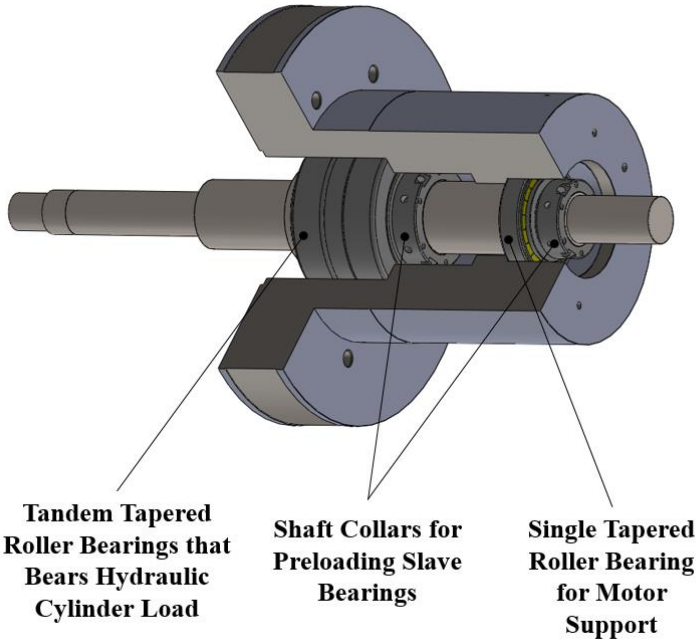

Figure 10 Spindle casing with bearings assembled model and notable features

The isolation flange acts as a barrier between the two chambers and prevents water contamination of the grease-lubricated slave bearings. The rotating shaft incorporates a mechanical shaft seal on the test bearing chamber side, which is capable of operating at 3600 RPM. Due to the non-zero leakage nature of the mechanical shaft seal, a 3D printed splash guard is installed on the slave bearing chamber side as a secondary seal. A small counterbore on the NDE of the slave bearing casing secures and aligns the splash guard.

A leakage relief channel machined into the isolating flange and test chamber casing provide a pathway out of the test rig for fluid leaking through the mechanical seal. An O-ring (#381) seals the OD of the isolating flange. Figure 11 shows a close-up view of the sealing configuration identifying critical components.

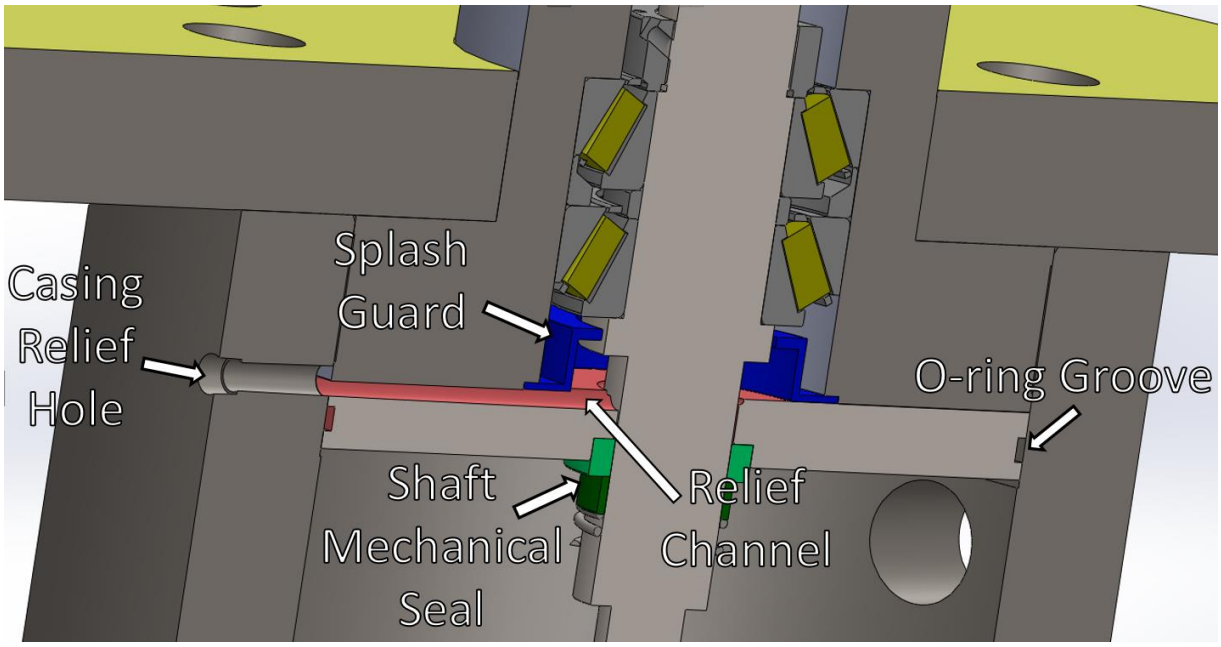

Figure 11 Test bearing and slave bearing chamber leakage isolation configuration

3.1.3 Test Rig Structure

The test rig structure supports the test rig in an upright position and facilitates the access to the test chamber. The support design is modular to allow for easy disassembly and reassembly of the test rig for relocation purposes (i.e. placement flexibility). Figure 12 shows an isometric view and sectioned cut-view of the structure.

The four columns of the structure bolt into the ground with vibration dampening concrete anchors. The top flat plate serves to support the motor while the second level flat plate, referred to as the support plate, connects to the spindle assembly of the test rig. The yellow and red X

shaped bars increase system stiffness and help elevate system natural frequency above operating conditions. Furthermore, removing one of the X members allows the use of a hydraulic hand lift that can grab the bottom portion of the test rig for convenient disassembly of the test chamber. This represents a critical feature of the design as there is the need to quickly and frequently access the test bearing without disassembling the entire rig. Figure 13 illustrates the assembly process.

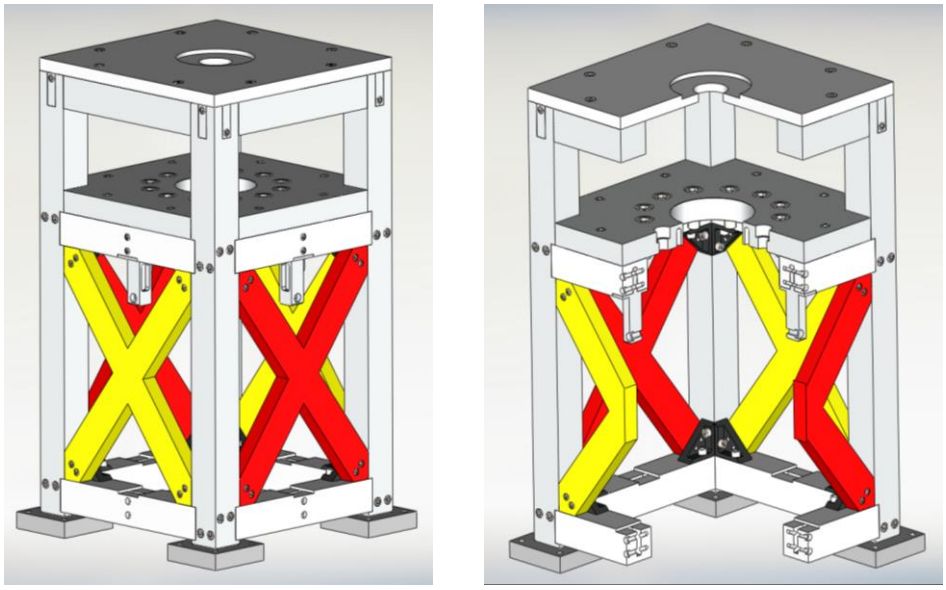

Figure 12 Test rig structure isometric view (left) and section cut view (right)

Figure 13 Test bearing assembly. The bottom assembly is lowered on the lift and pushed under the structure where it is raised into the test rig

3.2 Finite Element Validation

The design of both the rig itself as well as the test structure are validated using ANSYS finite element modeling. The analysis serves to evaluate the mechanical integrity of rig components during operation while the structure system analysis provided system natural frequencies and associated bending modes.

3.2.1 Test Rig Structural Deformation Evaluation

Figure 14 shows the fixed surface corresponding to the structure holding the rig in place, Figure 15 shows the 20,000 lbs force applied on the slave bearing chamber at the surface interfacing with the tapered bearings, as well as the reactive load of the same magnitude applied onto the plug inner face.

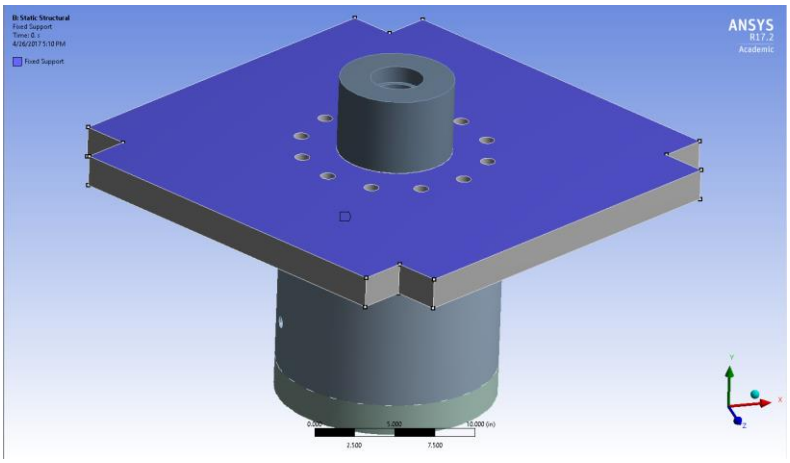

Figure 14 Fixed surface on the support plate in ANSYS deformation analysis

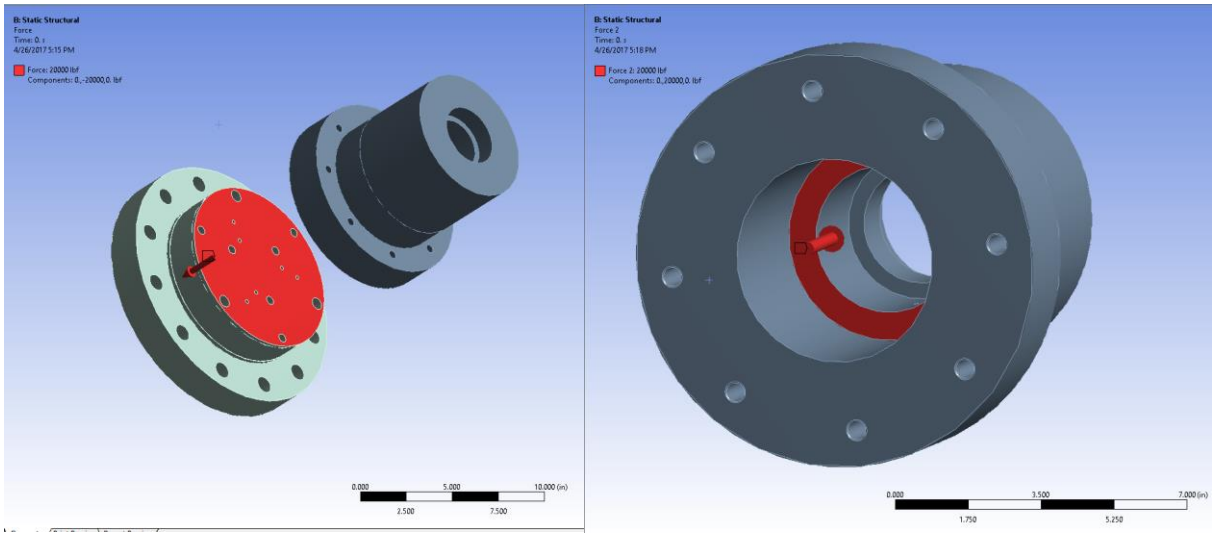

Figure 15 Applied forces on end plug (Left) and slave bearing housing (Right)

3.3 Leakage Path Considerations

There are 3 primary leakage paths in the test rig setup. First possible path, shown in Figure 16, is the connection between the bottom plug and the steel casing, which is static and sealed with an O-ring. The O-ring fits snugly inside a machined groove in the bottom plug and is pressed against the test bearing casing when the rig is fully assembled.

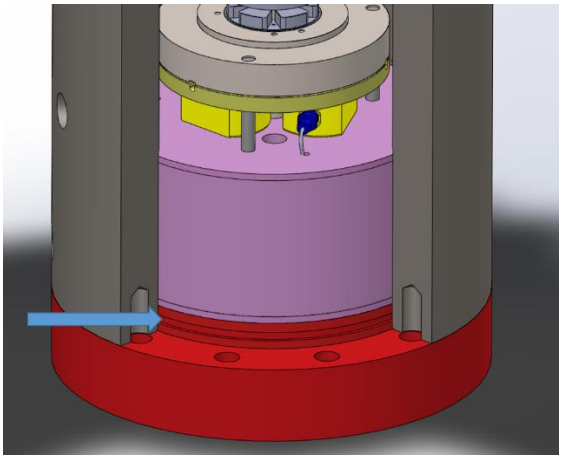

Figure 16 Bottom plug static leakage path. Arrow indicates O-ring placement

The second leakage path, illustrated in Figure 17, is the outer diameter of the interface between the test casing and the slave bearing casing and it is also sealed with an O-ring.

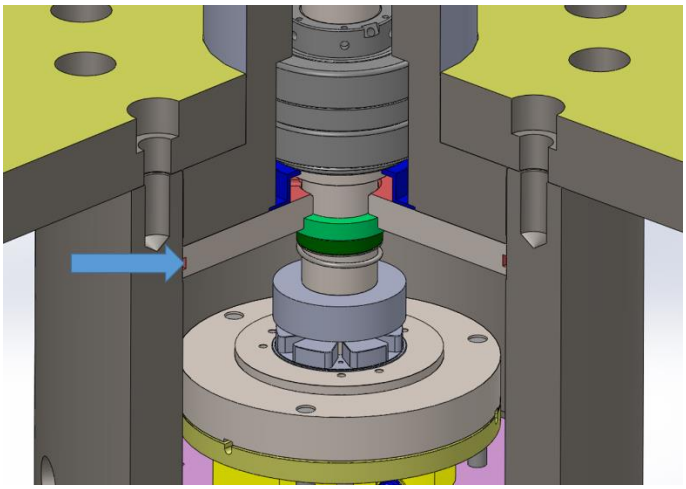

Figure 17 Test bearing chamber and slave bearing chamber seal. Arrow indicates O-ring placement

The third leakage path is at the inner diameter of the interface between the test casing and the slave bearing casing. Fluid could travel up through the ID of the isolating blind flange. A mechanical shaft seal is installed onto the shaft and pressed into the isolating blind flange to provide a dynamic seal interface. Due to the nature of mechanical shaft seals, some leakage is

bound to occur. To mitigate this, a plastic splash guard is implemented on the exit side of the seal. As mentioned in the previous section, a relief hole drilled onto the isolating blind flange provides an exit path for the fluid that moves past the seal.

3.4 Instrumentation

Instrumentation inside the test chamber include proximity probes, load cells, and RTDs while instrumentation outside of the test chamber include pressure transducers, a water flowmeter, and a torque meter. The instrumentation inside the chamber are routed out through water-tight feedthroughs on the bottom plug.

Three eddy current proximity sensors (120 degrees apart) embedded in the bearing plate face the thrust runner and provide an estimate of the film thickness by measuring the distance of the thrust runner relative to the bearing housing. The load cells are sandwiched between bearing plate and the load cell plate while radial holes inside the bearing pads house the RTDs. Two of the pads houses 3 RTDs each while the rest have slots for 1 RTD each for a total of 10.

A diaphragm pump delivers pressurized water to the test chamber and includes an actuation dampening accumulator to minimize pressure fluctuations. A nutating disk flowmeter in the inlet line measures the water flowrate. A valve at the exit of the test chamber regulates and increases the pressure delivered by the diaphragm pump. A contactless torque meter and tachometer combo is installed on the coupling connecting the motor and shaft for torque and power loss readings.

4. TESTING PROCEDURES & COMMISSIONING

This section details the commissioning of the test rig. While the current test rig is capable of operating with multiphase flow (water, sand and air), the scope of these tests is to demonstrate operability of the test rig and to provide preliminary data for two water-lubricated tilting pad thrust bearings constructed with distinct materials (PEEK and Tungsten Carbide -WC).

4.1 Test Bearings

Figure 18 displays the test bearings and Table 1 lists their dimensions. The Polymer and WC coated tilting pads bearings feature a steel pad support structure with an effective pad OD of 3.5" (8.89 cm). The pivot style is radial line contact and a small flat land region on the pivot allows the offset to be effectively 50% to allow bidirectional operation[1]. The tilting pad bearings includes a steel WC or PEEK coated flat face runner. Retainer screws maintain the relative position of the pads respect to each other and the back plate, while allowing tilting motion about the line pivot (2 degrees), as shown in Figure 19.

Figure 18 Picture of PEEK and WC wafer test bearings

[1] While ESPs are designed to operate in one direction, the sponsor of the project indicated that there are many instances in the field when these pump are accidentally operated in reverse during start up or due to well conditions (backflow).

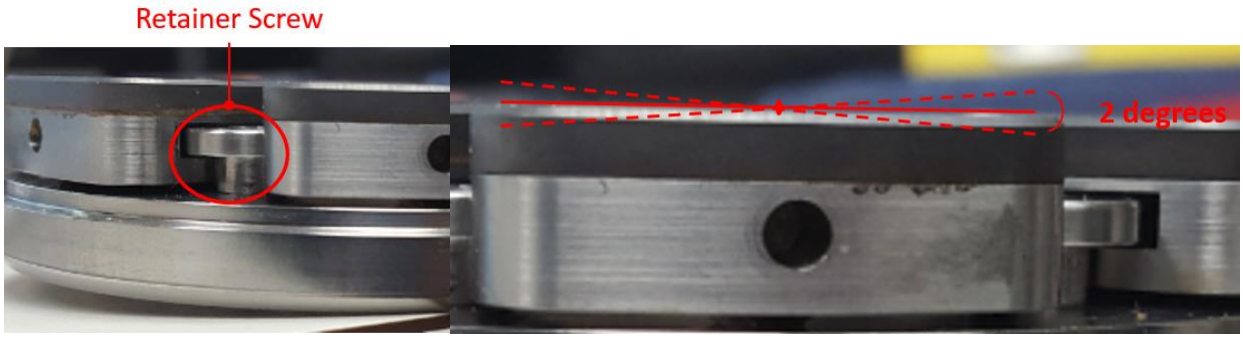

Figure 19 Retainer screw location and tilt angle of bearing pad

Inner Diameter	1.6” (4.06 cm)
Outer Diameter	3.5” (8.89 cm)
Pad Length	0.97” (2.46 cm)
Pad Width	0.97” (2.46 cm)
Arc Length	1.14” (2.90 cm or 39˚)

Table 1 Test Bearing Dimensions

The unit load of a bearing is calculated by dividing the applied load over the surface area of the bearing. The surface area of the bearing is defined as the continuous highlighted region shown in Figure 20.

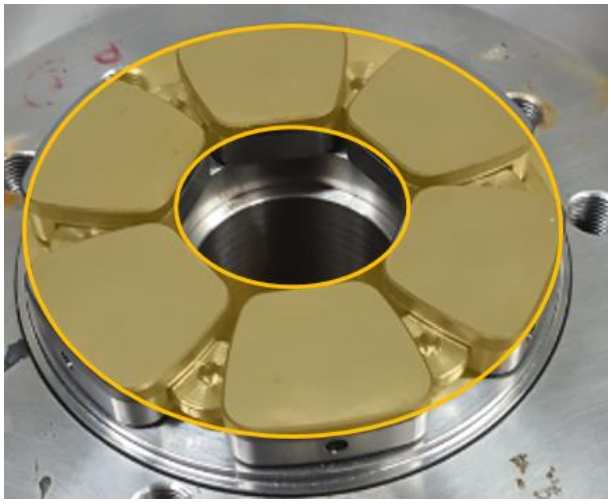

Figure 20 Surface area of a WC tilting pad test bearing

4.2 Test Procedure

Figure 21 shows the test matrix and outlines test procedures. The first experiments are forward drag torque and power loss static performance tests. The tests start by spinning the motor to the desired speed and increasing the applied load (at an approximate hand controlled rate of 6 lbs/s) until a temperature spike is recorded in the pads (i.e. a sign of hard contact). The tests serve to determine the bearing load capacity just before the hydrodynamic fluid film collapses. Upon finding the maximum unit load, a wear test follows by subjecting the bearing to 105% of the previously determined load. This is done to determine if the bearing can feasibly operate beyond the hydrodynamic limit. Inspections are performed after every 5 hours to examine the amount of wear on the pad and runner. The purpose of this test is to determine if the wear rate is low enough to allow continuous operation at the set unit load.

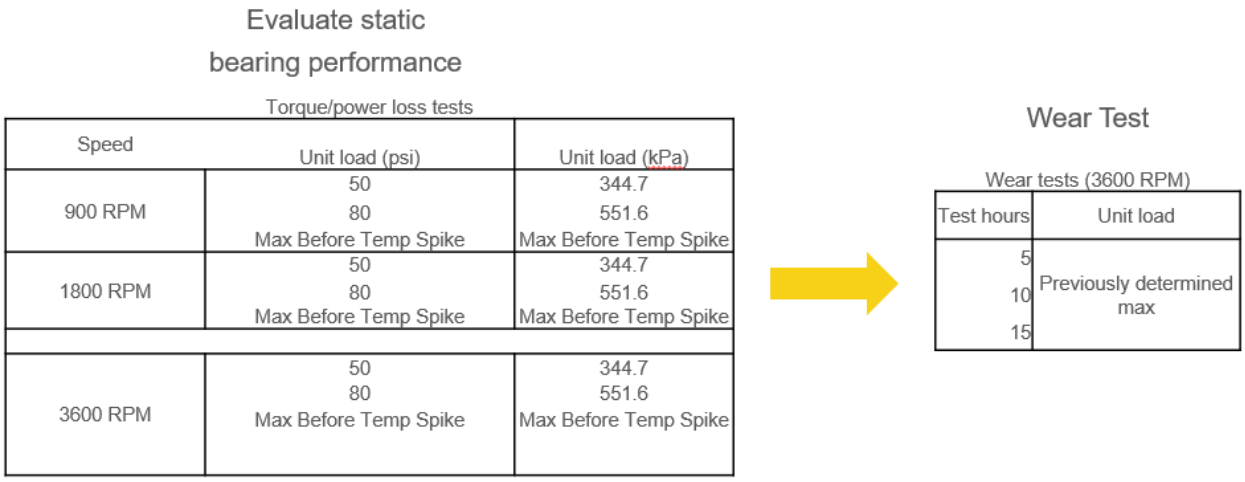

Figure 21 Test matrix for WC and PEEK tilting pad bearings

The bearing test rig start-up sequence begins by turning on the air driving the diaphragm pump and setting the chamber pressure by regulating air supply pressure to the pump and partially closing the test rig outlet valve until the chamber pressure is at a desired 40-50 psig (0.27 to 0.34 MPa). Operation of the motor through the VFD follows the chamber pressurization. An operator acts the loaders until reaching the desired load. The DAQ system records the data from the sensors during the startup sequence and after reaching steady state operation. Measurements include temperature, torque, load, flowrate, chamber pressure, and film thickness.

4.3 Procedure Changes & Commissioning

Several changes were made to the test procedure as the rig was commissioned. First, three pads were removed from the initial six pad bearing because the bearing was not able to hold a consistent fluid film even at zero load conditions once the motor was running. The hypothesis for this phenomenon is lubricant starvation due to a lack of an unrestricted flow path/access to the inner diameter of the bearing. The natural outward-pumping action of the

bearing creates a natural flow path from the inner to the outer diameter of the thrust runner. If there is not enough volume of lubricant to consistently resupply the bearing, the film will starve leading to boundary or mix lubrication. It is suspected that this was the case since the shaft occupies most of the bearing ID and the bearing is simply submerged in the lubricant (i.e. there is no direct injection).

Two 6-pad (PEEK and WC) bearings experienced rubbing almost immediately the moment any load was applied. The PEEK coating was destroyed while the WC coating experienced heavy wear. Figure 22 and Figure 23 show pictures of the bearings after testing with the six pad configuration. Note that in Figure 23, the heavily worn side of the bearing pad is actually on the leading edge of the fluid film as indicated by the runner rotation direction. This also suggests that the pad was not properly lubricated (fluid starvation).

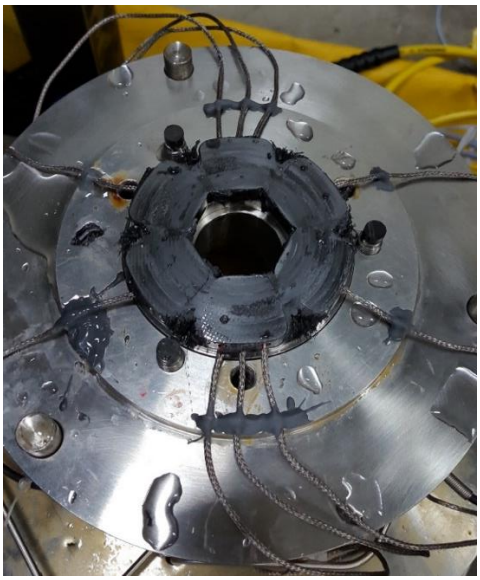

Figure 22 PEEK bearing damaged during testing. Only 100 psi of unit load was applied.

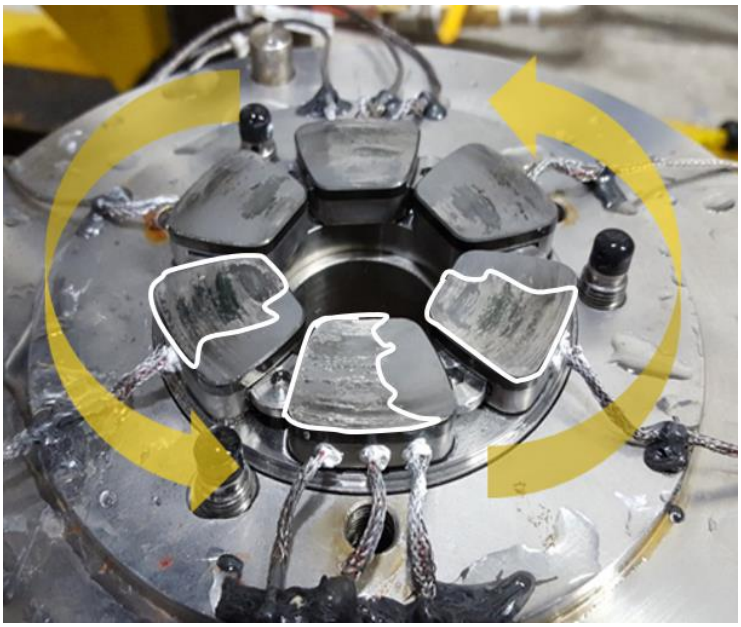

Figure 23 Heavily damaged WC bearing. Arrows indicate rotation of the runner. Leading edge of the pads are outlined in white

A light microscope allowed inspection of the wear intensity on the starved WC bearing as shown in Figure 24. The wear is not uniform as the leading edge experienced much more intense rubbing than the exit region, which appears to be relatively untouched. The pattern of erosion and the absence of particles indicate this wear type resulted from two body abrasion.

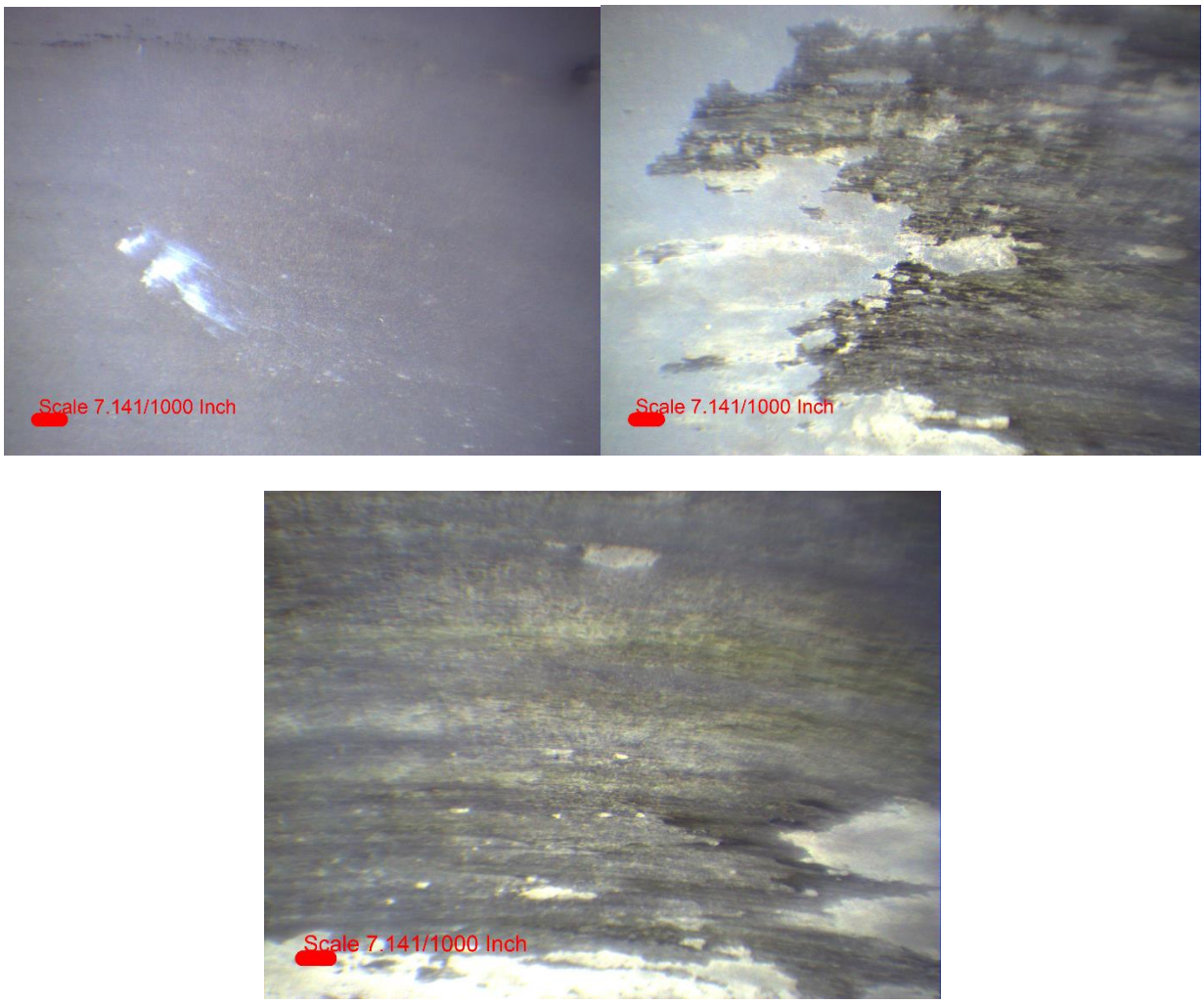

Figure 24 Magnified wear pattern for a lubrication starved WC bearing (pad 2). Top left: trailing edge of pad. Top right: middle of pad. Bottom: leading edge of pad.

Figure 25 shows the magnified wear on PEEK pad surface. The PEEK material wore out much faster than WC since it is a softer material and was rubbing against a WC coated runner. As a result, most of the PEEK liner was sheared off leaving only the steel substrate below it.

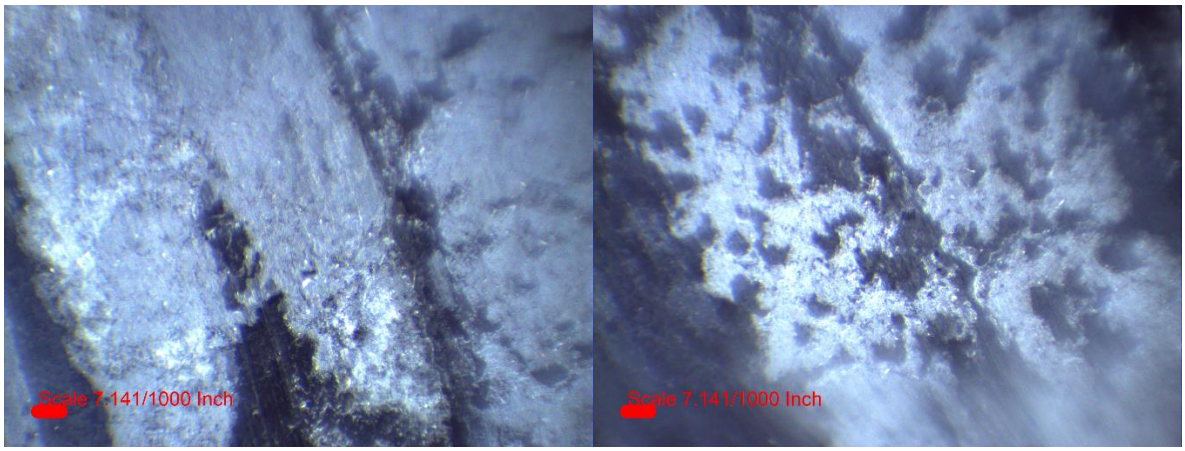

Figure 25 Magnified wear pattern in the middle of the pad for a lubrication starved PEEK pad. Much of the PEEK material has been worn away, leaving the steel substrate exposed

A simple solution to prevent film starvation without modifying the test rig is using three pads to provide free path for the fluid to reach the inner diameter of the bearing pads as well as pressurizing the chamber slightly. After these modifications, the bearings were able to hold much more load at the same speed and thus corroborating the fluid starvation hypothesis.

Due to the low torque of the motor (80 Nm or 59 ft-lbs), testing the WC bearing to failure could not be accomplished. Applying too much load to the bearing will simply cause the test rig to seize and the shaft safety coupling, which disengages the motor from the rig when a sufficiently high torque is reached, to trip. However, it was later determined that boundary lubrication operation for the WC bearings is not sustainable.

5. RESULTS & DISCUSSION

5.1 Experimental Results for WC

Tests for the 3-pad WC wafer bearings follow the test matrix outlined in Figure 21. All testing featured a chamber pressure of 40 psig (0.4 MPa) and a flowrate of 8 ± 1 GPM (39.2 liters per minute) in bath lubrication.

5.1.1 Experimental Results at 900 RPM

At 900 RPM (4 m/s surface speed) with proper lubrication, both torque and temperature show marginal increases until contact occurs. The results are shown in Figure 26 and Figure 27. The torque and power loss associated with a zero-load condition in Figure 27 correspond to the torque generated by the slave tapered roller bearings. This baseline case is subtracted from subsequent measurements with load to obtain the torque generated by the test bearing.

The temperature rise seen in Figure 26 is fairly flat in the hydrodynamic regime until contact occurs, in which case a sudden increase occurs. This is consistent with XLThrustB code predictions of low pad temperature rise in water lubrication. The average temperature is defined as the mean temperature of the leading edge, trailing edge, and center of every pad.

The torque graph shown in Figure 27 shows less variation in the hydrodynamic regime than the torque graph for the 3600 RPM case (Figure 36). This is likely due to the lower operating speed which causes less rubbing. As expected, the uncertainty increases once rubbing does occur. The maximum unit load before a film begins collapsing is approximately 210 psi (1.24 MPa) and is marked on Figure 27.

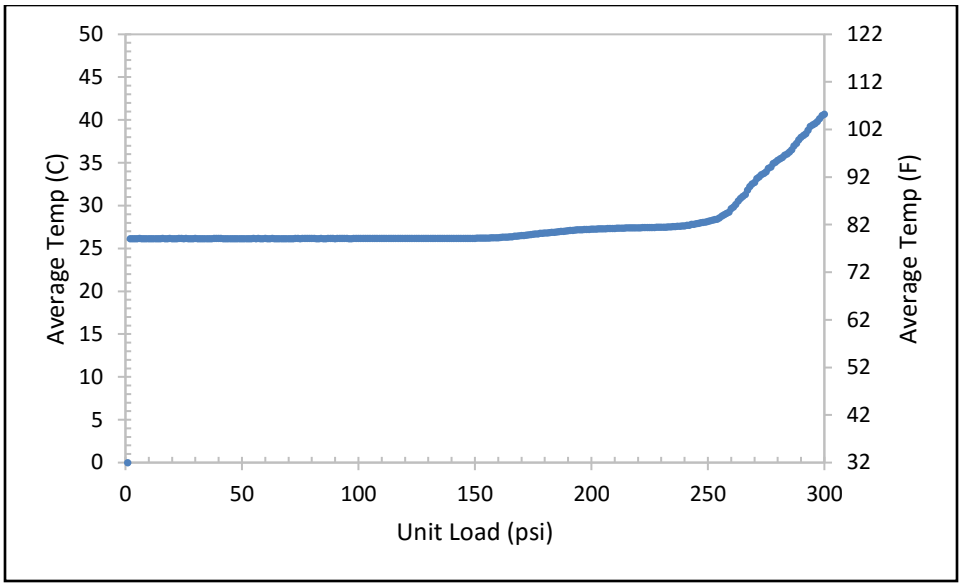

Figure 26 Average temperature in the pads vs unit load for WC wafer at 900 RPM

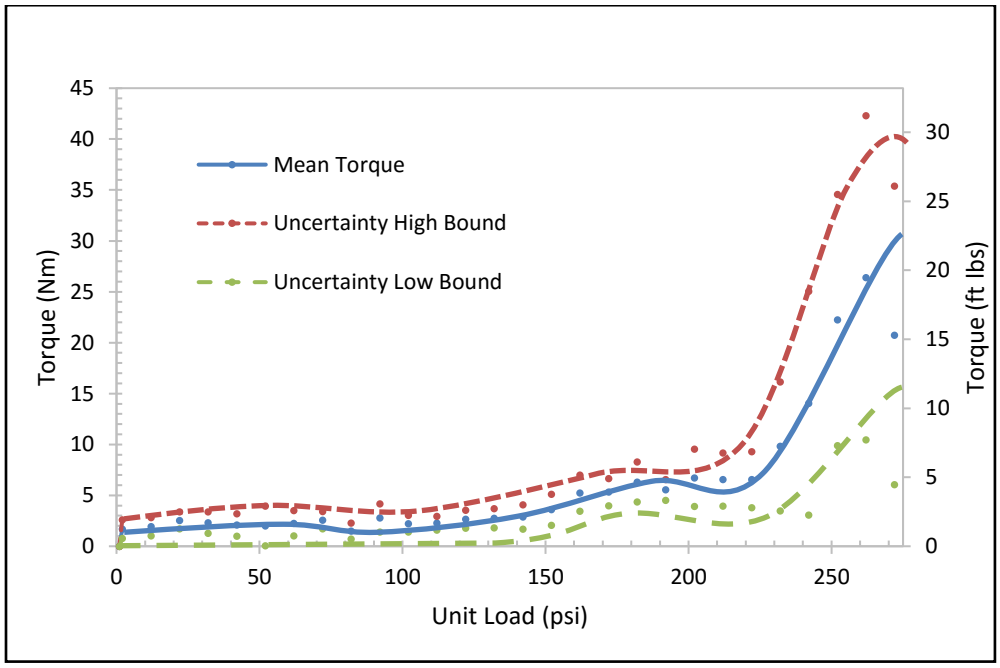

Figure 27 Torque vs unit load for WC wafer at 900 RPM

At approximately 220 psi (1.51 MPa) unit load for shaft speed of 900 RPM, a spike in pad temperature is detected. Upon disassembly and examining the pads, wear streaks can be seen

as pictured in Figure 23. The wear is more significant on the leading edge of the bearing pad, which suggests that when contact occurred, the fluid film broke and the pads contacted the runner.

Figure 28 shows the friction coefficient versus the unit load at 900 RPM. The friction coefficient is calculated by dividing the torque over applied load and mean radius of the bearing. The graph shows three distinctive trends of the viscosity that are qualitatively identified as a hydrodynamic, mixed and boundary lubrication regions. In the hydrodynamic region the friction coefficient decreases as the load increases, which indicates torque is relatively constant and the bearing is operating without contact between runner and pads. The mixed lubrication region displays a modest increase in friction coefficient as the unit load increases, which is associated with a torque increase due to initial asperity contact between the stationary and rotating surfaces. The final region is characterized by an increase of the friction coefficient rate of change respect to unit load, coinciding with a sudden increase of the input torque and pad surface temperature (i.e. film rupture).

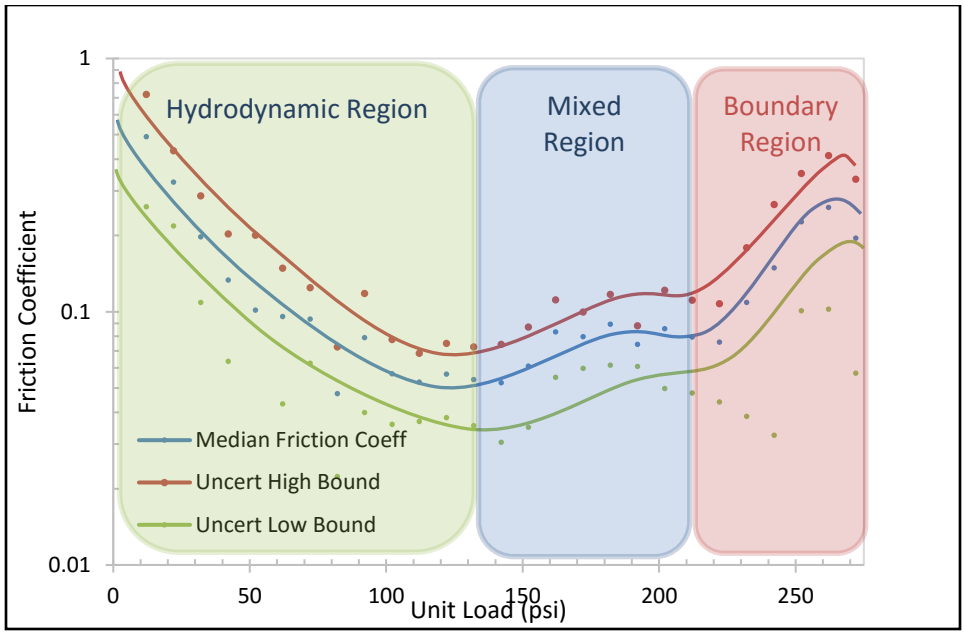

Figure 28 Friction coefficient vs unit load for WC at 900 RPM. The hydrodynamic and mixed lubrication region are marked as green and blue regions respectively.

Figure 29 depict observations under a light microscope showing that the damage incurred on the bearing is indicative of sliding wear and that the pads are not uniformly worn but rather damaged more heavily on one side than the other. In fact, the undamaged side (the trailing edge) barely shows any wear at all; however, the damage when using three pads is notably less severe than the damage incurred when using all six pads, as shown in Figure 24. This further corroborates the lubrication starvation hypothesis.

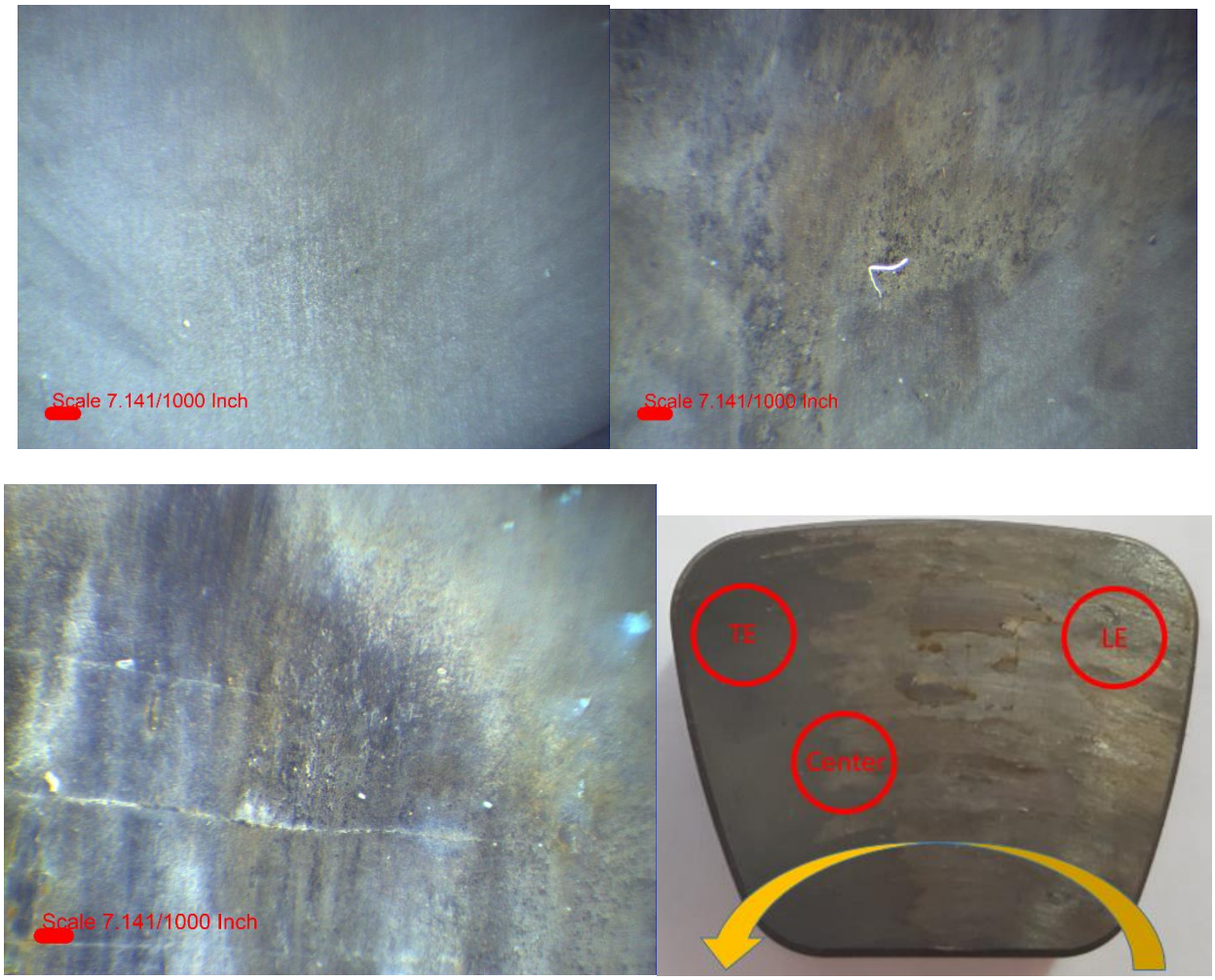

Figure 29 Microscopic views of wear on WC bearing pad 1. Top left: trailing edge. Top right: pad center. Bottom left: leading edge. Bottom right: pad locations with direction of rotation

5.1.2 Experimental Results at 1800 RPM

As the speed of the shaft increases, the bearing can withstand more unit load. At 1800 RPM (surface speed of 8 m/s), the max tolerable unit load before rubbing occurs at approximately 250 psi (1.72 MPa). Figure 30, Figure 31, and Figure 32 show the average temperature, torque and friction coefficient vs unit load, respectively. Once again, the average temperature is the mean temperature of the trailing edge, leading edge, and center of all the pads.

The trends are similar to the 900 RPM case in that both temperature and torque stay relatively flat until contact occurs, in which both graphs experience a spike.

The friction coefficient, pictured in Figure 32, follows a similar trend defining three characteristic lubrication regions as that described for the 900 RPM case.

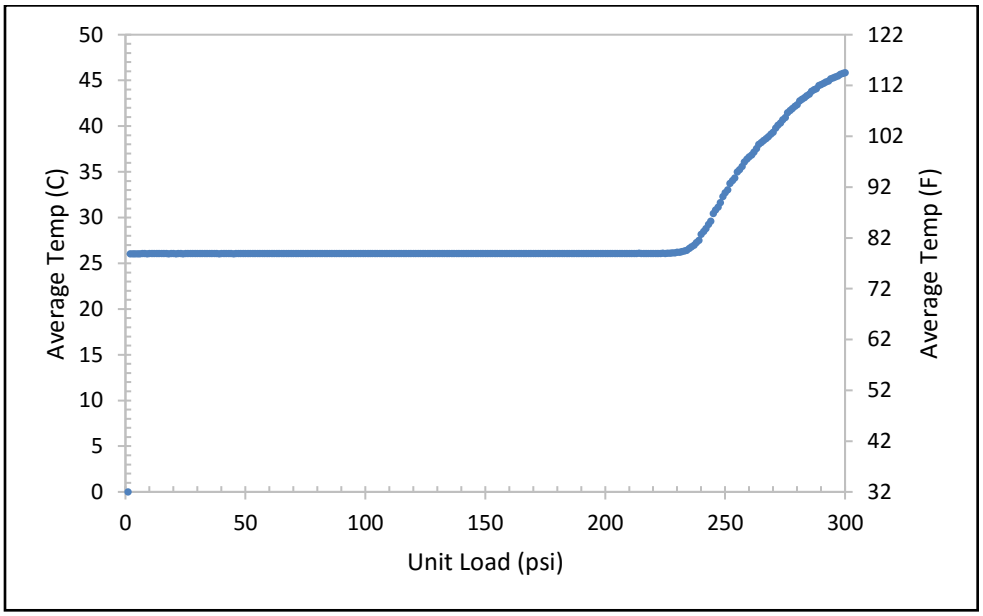

Figure 30 Average temperature vs unit load for WC wafer at 1800 RPM

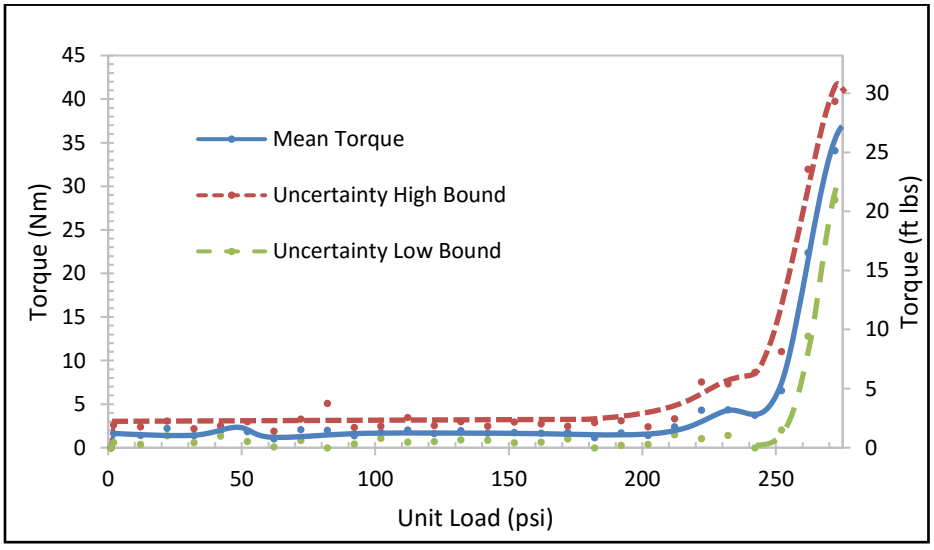

Figure 31 Torque vs unit load for WC wafer at 1800 RPM

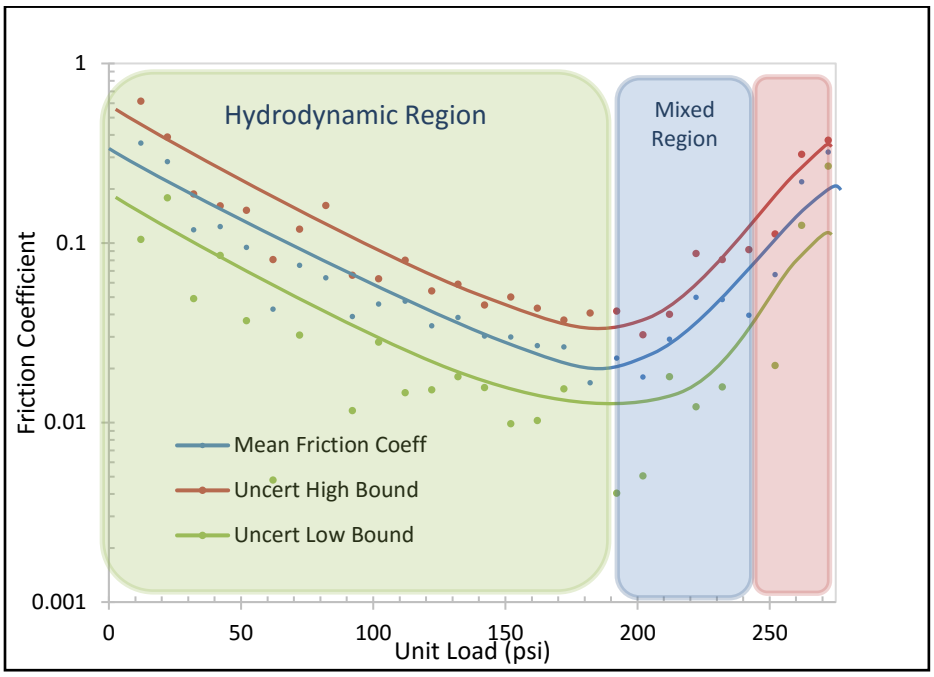

Figure 32 Friction coefficient vs unit load for WC wafer at 1800 RPM. Hydrodynamic and boundary regions are marked green and blue respectively.

Upon inspection, wear follows the same pattern (higher at the leading edge, lower or untouched at the trailing edge) as in the 900 RPM case. Microscope inspection of the pads, seen in Figure 33, show the same type of two body sliding wear as seen in the 900 RPM case. The heavily worn leading edge region experienced much more wear than the lubricant exit region which barely experienced any wear at all. Once again, the wear intensity is less severe than as in the lubricant starved case.

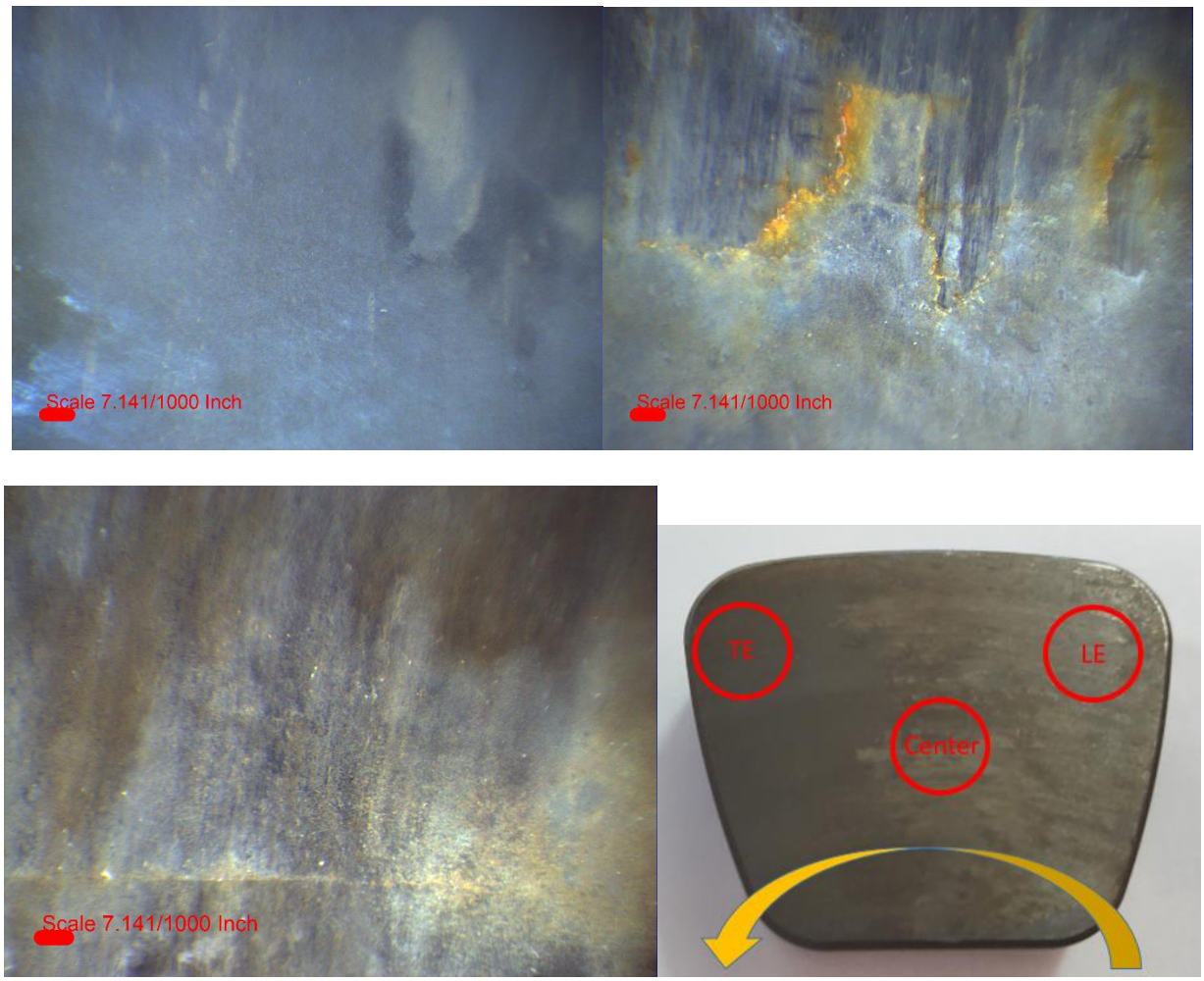

Figure 33 Microscopic views of wear on WC bearing pad 3 for 1800 RPM. Top left: trailing edge. Top right: pad center. Bottom left: leading edge. Bottom right: pad locations with direction of rotation

5.1.3 Experimental Results at 3600 RPM

Operation at 3600 RPM (surface speed of 15 m/s) yielded the highest hydrodynamic unit loads before rubbing. A temperature spike in the pads did not occur until the unit load magnitude reached 350 psi (2.41 MPa). This value represents the maximum load carrying capacity for continuous operation.

Though the test rig is outfitted with proximity probes, film measurements are not currently available due to high measurement variability in the initial tests as well as premature failure of the probes during the 6-pad bearing testing.

Average temperature for operation at 3600 RPM exhibits a constant magnitude during full hydrodynamic operation, as shown in Figure 34. Rubbing occurred at approximately 350 psi (2.41 MPa) unit load as there was a notable jump in pad temperatures at that point. This is notably larger than the hydrodynamic limit of 130 psi (0.89 MPa) at 900 RPM. Figure 35 shows pad temperature versus pad position. Generally, the temperature at the pad exit is the hottest until the fluid film breaks completely. When this occurs, the leading edge of the pad is dragged with the runner and experiences higher temperatures than the rest of the pad. Temperature decreased briefly when the unit load increased from 480 to 550 psi (3.3 to 3.79 MPa). This trend may be related to a slight tilt in the bearing orientation due to pressure redistribution in the hydraulic cylinders. The error band in the temperature graph is too small to be displayed (approximately 0.5 C).

Torque measurements depicted in Figure 36 exhibit a fairly steady low torque in the 2.5 Nm (1.84 ft-lbs) range until 350 psi (2.41 MPa) unit load is reached. Afterwards, a spike in torque occurs as the bearing begins rubbing with the runner. The high torque in the early hydrodynamic regime is likely a contribution from ancillary elements in the test rig unrelated to the test bearing that were not properly baselined. The torque measured in the hydrodynamic range (low unit loads) is same for all speeds and thus independent of running speed.

Figure 37 shows the friction coefficient displaying, as in previous cases, three distinctive regions associated to different lubrication regimes. The boundary lubrication region can be seen as load was continually applied even after contact occurred. In this particular case, as the load

was further increase, the friction coefficient stabilizes to a constant value, which may be associated with the removal of the thrust collar WC coating layer and increase of material removal rate.

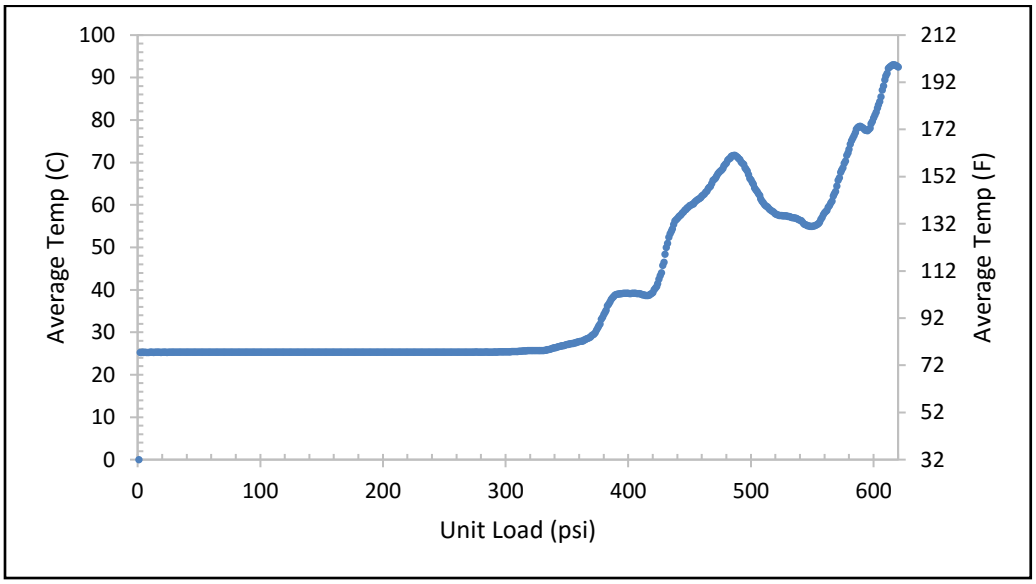

Figure 34 Average temperature vs unit load for WC wafer at 3600 RPM

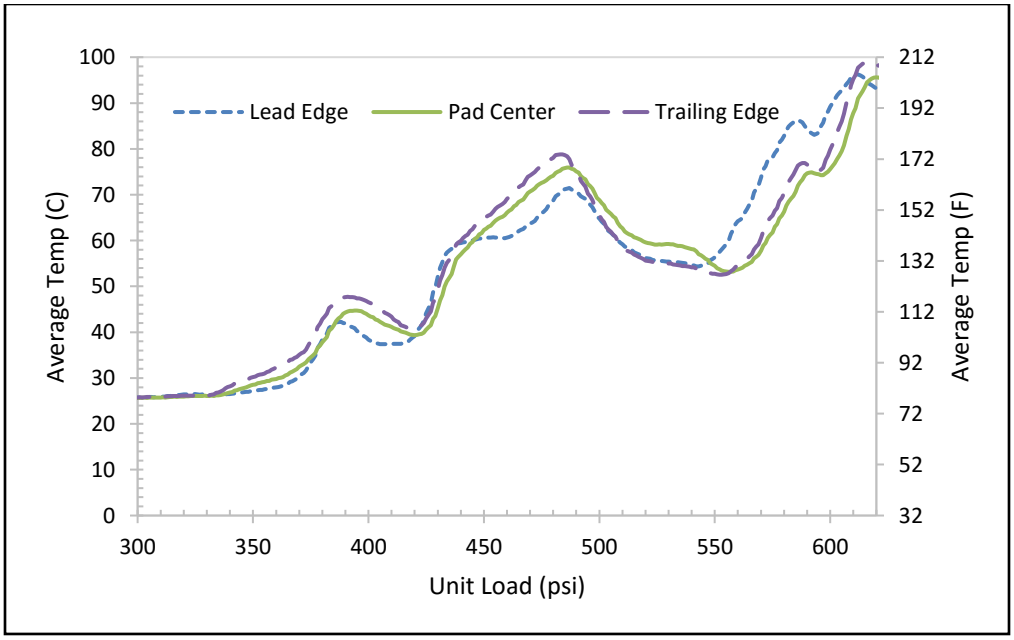

Figure 35 Pad position temperature vs unit load for WC wafer at 3600 RPM

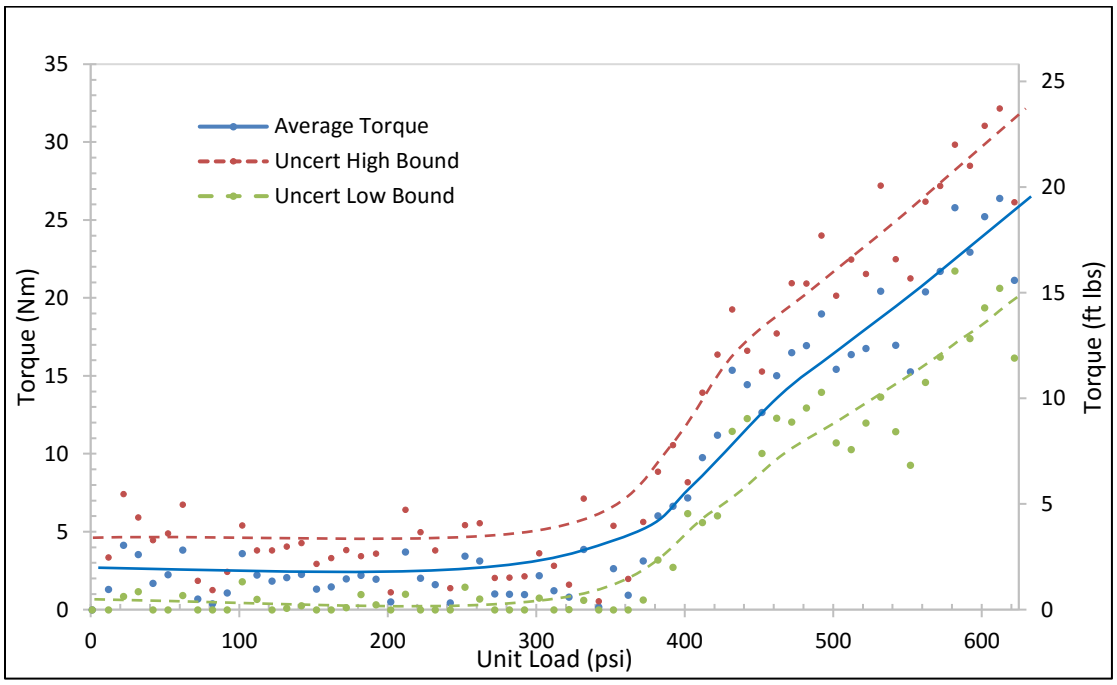

Figure 36 Torque vs unit load for WC wafer at 3600 RPM

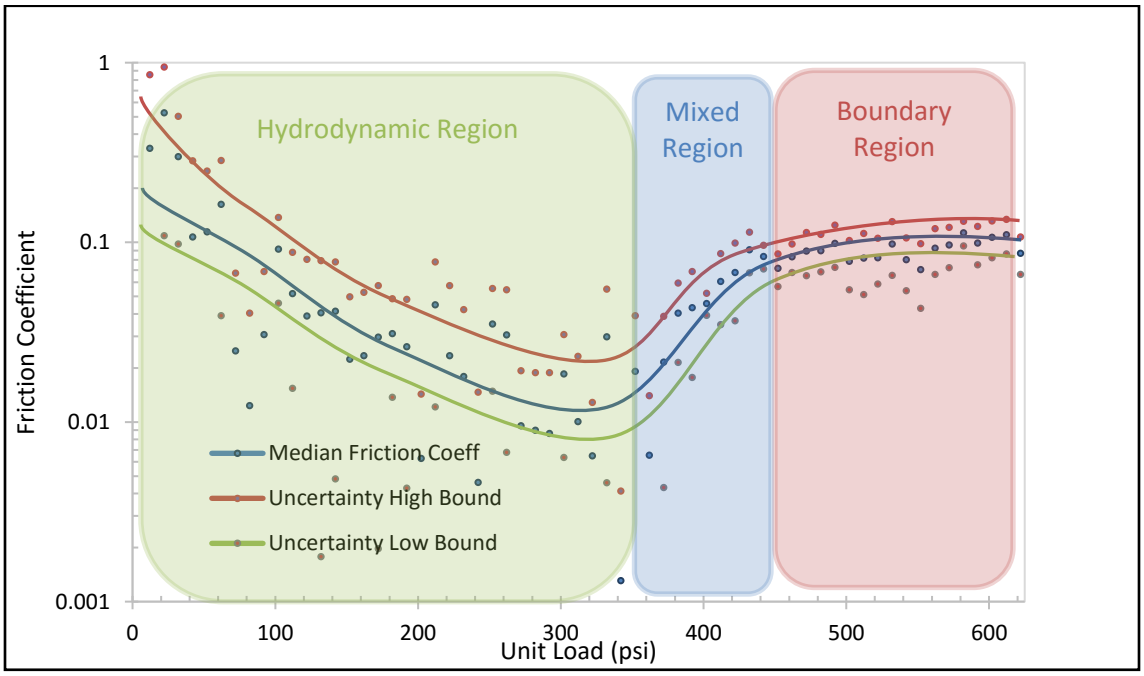

Figure 37 Friction coefficient vs unit load for WC wafer at 3600 RPM. The hydrodynamic, mixed, and boundary lubrication regions are marked green, blue, and red respectively.

Figure 38 shows the thrust bearing and collar after disassembly. The bearing pads display significant wear but mostly concentrated at their leading edges. The source of rust is the 17-4 PH stainless steel runner. This type of martensitic steel is not truly stainless as it does not contain chromium and can rust when exposed to atmospheric conditions. Initially, a coating of WC on the surface of the runner prevents it from rusting; however, the coating wore off during testing which exposed the bare 17-4 PH steel to water. Some of the 17-4 PH steel deposited on the bearing pads and none of the rust originated from the WC wafer. Figure 39, which shows the cleaned up bearing from Figure 38, displays the shaft rotation and the wear patterns. It is important to note that the wear mostly concentrates on the leading edge of a bearing pad. This is a symptom of pad starvation and fluid film breaking, which corroborates the torque readings.

Figure 40 depicts a close-up view of the pad surface using a light microscope. Patterns of wear show more damage at the leading edge of a pad. Some amount of rust is present at the wear boundary, likely deposited from the runner. The microscope image in Figure 40 show less material removal when compared to the images shown in Figure 24, which indicates that the wear intensity of the 3600 RPM case is less severe than that resulting from bearing lubricant starvation.

Figure 38 Left: WC bearing post 3600 RPM static test. Right: steel runner after testing. Source of rust is the 17-4 PH stainless steel runner.

Figure 39 Direction of rotation shown in yellow vs wear pattern for WC bearing. White region denotes leading edge.

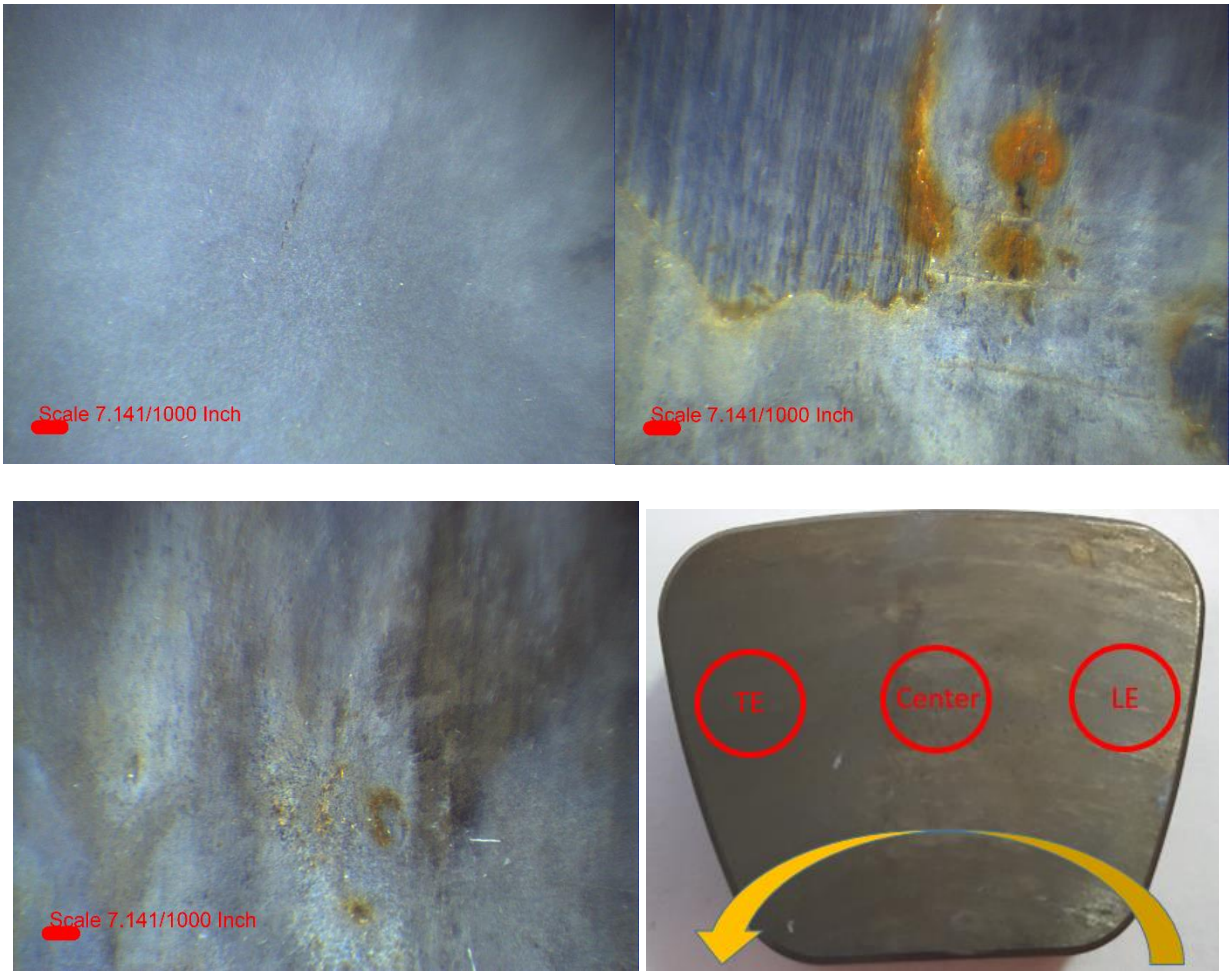

Figure 40 Microscopic views of wear on WC bearing pad 2 for 3600 RPM. Top left: trailing edge region. Top right: middle of pad. Bottom left: leading edge. Bottom right: pad locations with direction of rotation

The next set of tests aimed at evaluating the hydrodynamic and temperature stability of the WC bearing when operating at the hydrodynamic operation maximum unit load (i.e. before reaching boundary lubrication). The tests spanned 5 hours with unit loads ranging from 300 to 350 psi (2.06 to 2.41 MPa). Figure 41 plots the unit load applied vs time which remains fairly steady throughout the 5 hours. The temperature of the pads, as shown in Figure 42, did not spike during these 5 hours suggesting no rubbing occurred.

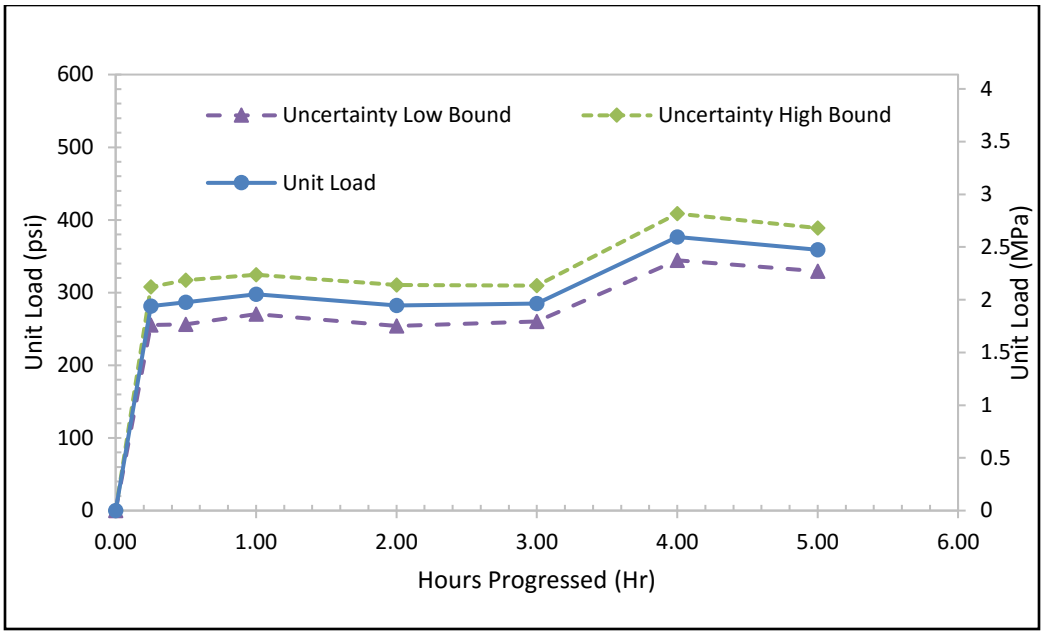

Figure 41 Unit load applied vs time for the WC wafer hydrodynamic test at 3600 RPM

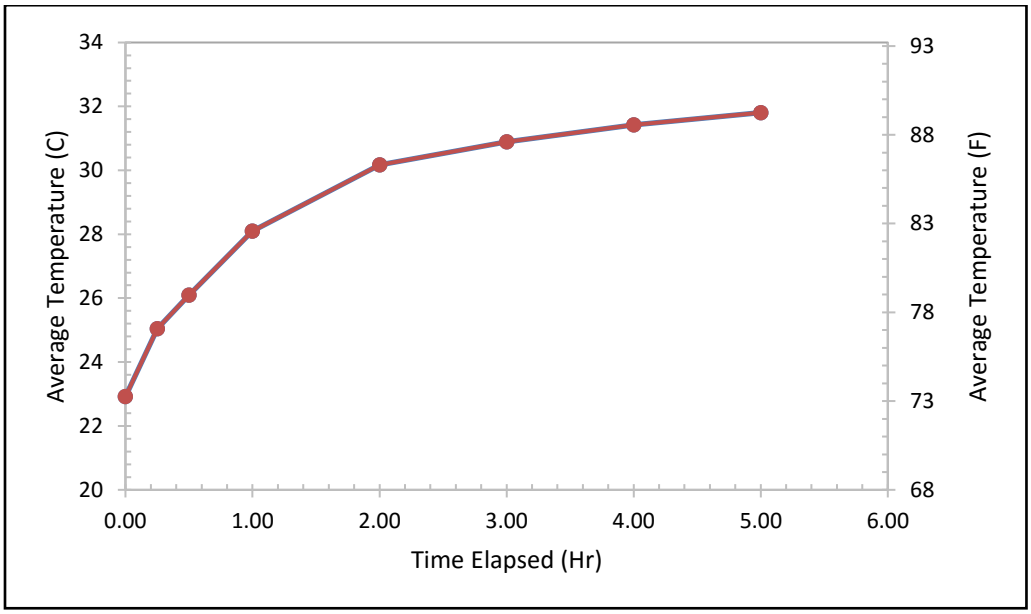

Figure 42 Average temperature in the pads vs time passed for the WC hydrodynamic test at 3600 RPM.

Upon disassembly, both the runner and the bearing pads showed no signs of wear indicating the bearing operated under a full hydrodynamic mode. A closer inspection with the light microscope

of pad center, shown in Figure 43, reveal small streaks on the surface of the pad along the circumferential direction. However, wear is minimal to the point that even the thin layer of polymeric coating on the WC wafer was not removed, which is indicative of mixed lubrication operation (surface asperity contact).

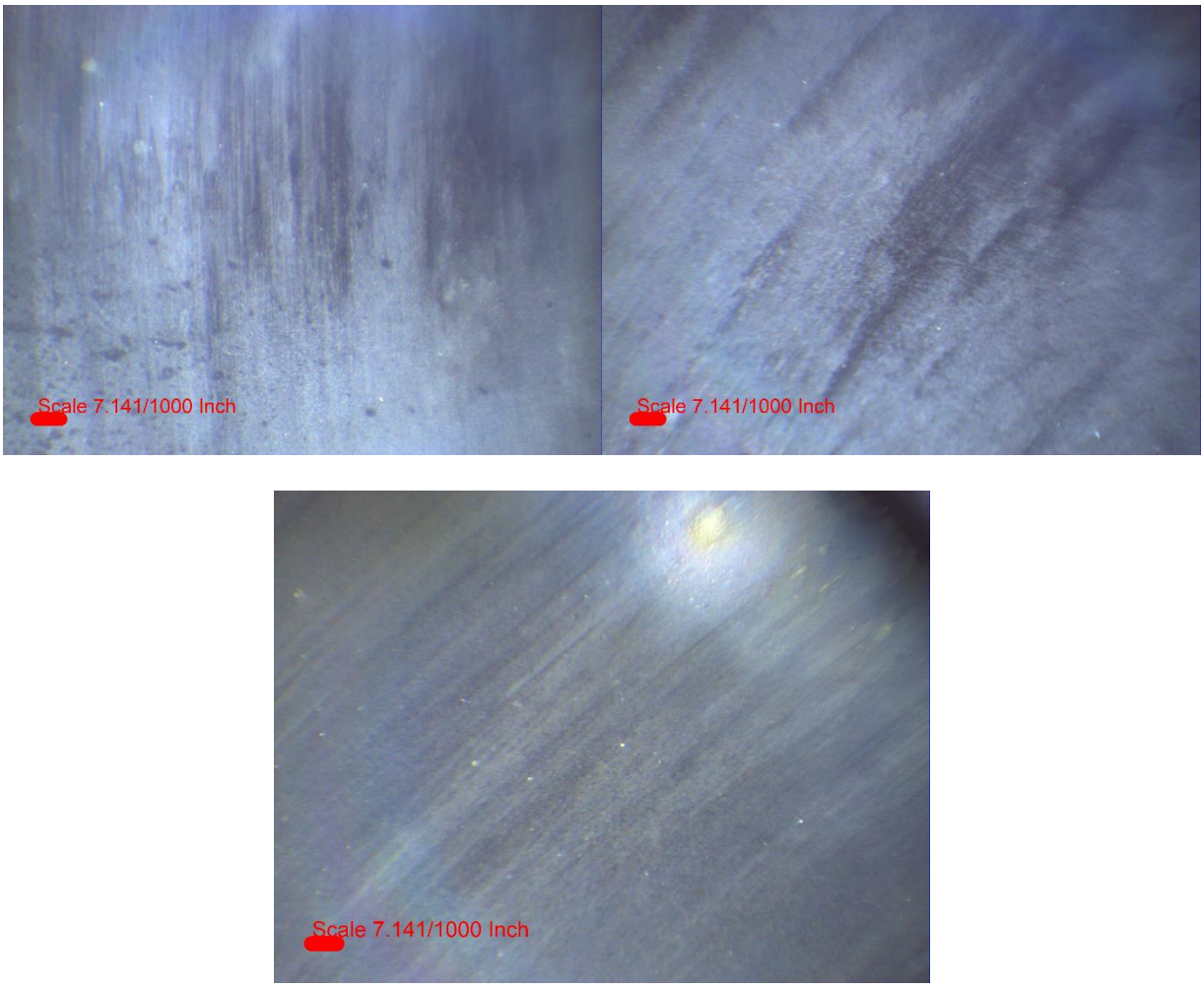

Figure 43 Microscopic view of wear on WC bearing pad for 3600 RPM. Top left: pad 1. Top right: pad 2. Bottom: pad 3. No appreciable wear can be seen

5.2 Modeling Results for WC in XLTRC

The XLTRC2 program, XLThrustB, predicts the film thickness, torque, temperature distribution, deformation of a thrust bearing among other parameters that can corroborate test results. Table 2 lists relevant input parameters.

Parameter	**US Units**	**SI Units**
Fluid Viscosity	1 cP for water, 35 cP for ISO VG 32	1.5 mPa·s for water, 35 mPa·s for ISO VG 32
Supply Temperature	68° Fahrenheit	20° Celsius
Load Range on Bearing	45-1,210 lbs	200-5400 N
Unit Load Range on Bearing	14-400 psi	0.1-2.78 MPa
Operating Speed	3600 RPM	
Surface Speed	53 ft/s	16.13 m/s
Pivot Offset	60%	

Table 2 XLThrustB input parameters

Figure 44 shows the film thickness versus specific load for both water and ISO VG 32 lubricated bearing. Predicted film thicknesses is on the order of 0.6 mils for ISO VG 32 and 0.2 mils for water at 350 psi (2.41 MPa) unit load. The film thickness for oil is notably larger than water as expected due to the higher viscosity. Due to the thin film thickness in the water lubricated case, surface damage caused by axial vibrations or start-up or shut down could potentially cause film breaking and intermittent contact. If the surface roughness were to exceed 5 microns, this could potentially cause the bearing to exit hydrodynamic regime and enter boundary lubrication.

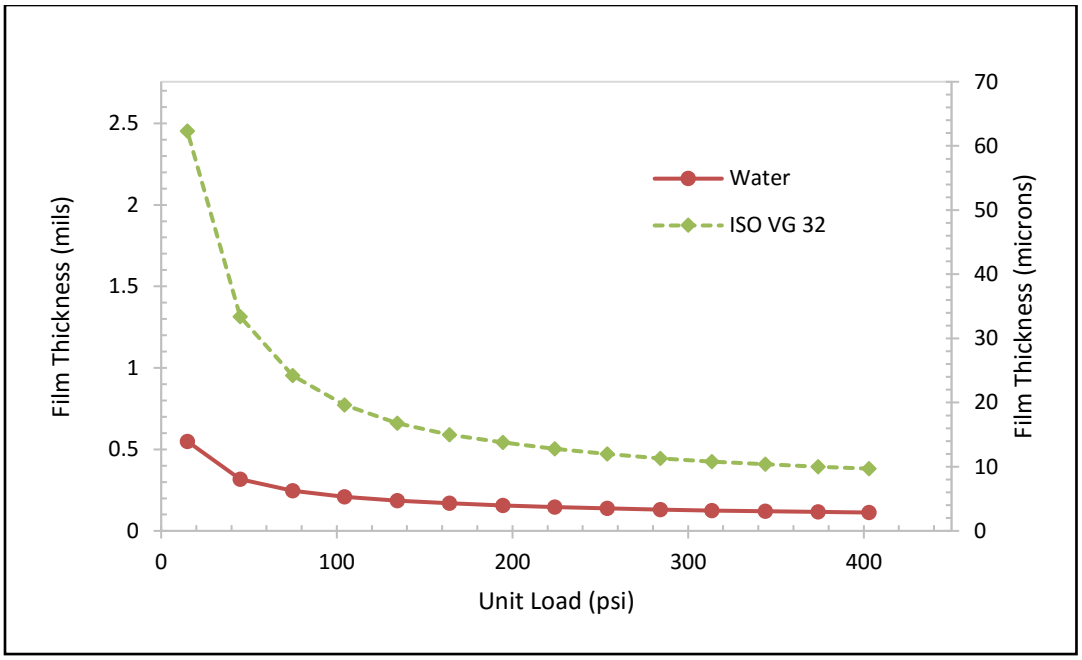

Figure 44 Film thickness vs specific load for water and ISO VG 32

The temperature rise in the pads from experiment correlate well to predictions, as seen in Figure 45. Predictions indicate a temperature rise of only 6 C at a unit load of 400 psi (2.76 MPa), which is a relatively small increase when compared to the 27 C predicted increase from ISO VG 32. Experimental temperature data in the hydrodynamic range corroborates this prediction as there is no significant temperature rise in the hydrodynamic region of 0-350 psi (0 to 2.41 MPa) unit load. The lower temperature rise in the pads is due to water's high heat capacity which allows it to whisk and carry heat away better than oil. Discrepancy at the 350 psi (2.41 MPa) unit load region arises due to the fact that rubbing has occurred in the actual pad, whereas predictions still assume a full hydrodynamic regime with less than 0.2 mils of film thickness.

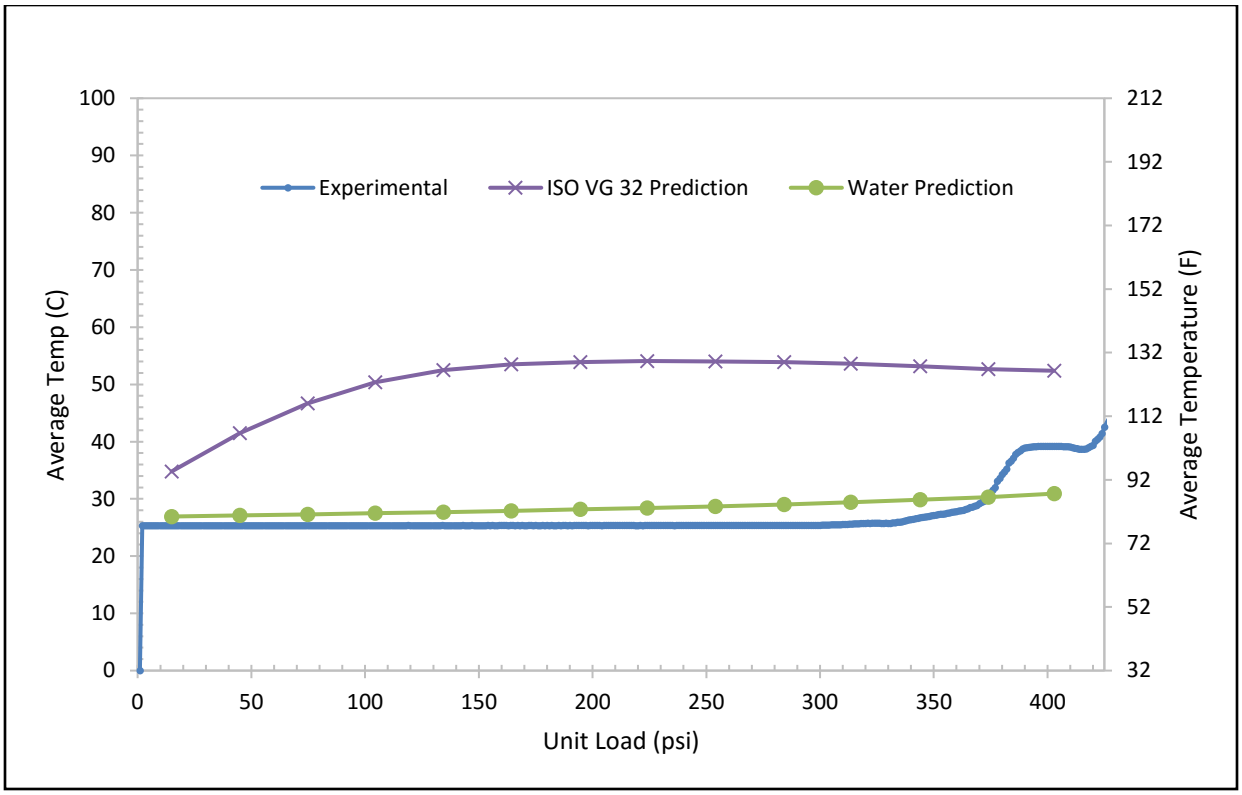

Figure 45 Average temperature increase; predictions vs experiments for water and ISO VG 32 lubricated bearing

Torque predictions versus experimental data are shown in Figure 46. Simulation predicts smaller torques in the hydrodynamic range than what the experimental results show. This is likely due to churning losses not properly baselined in the experimental case and intermittent contact as the predicted film thickness in pure water lubrication is on the order of 0.1 to 0.3 mils (2.54 to 7.62 microns) (Figure 44).

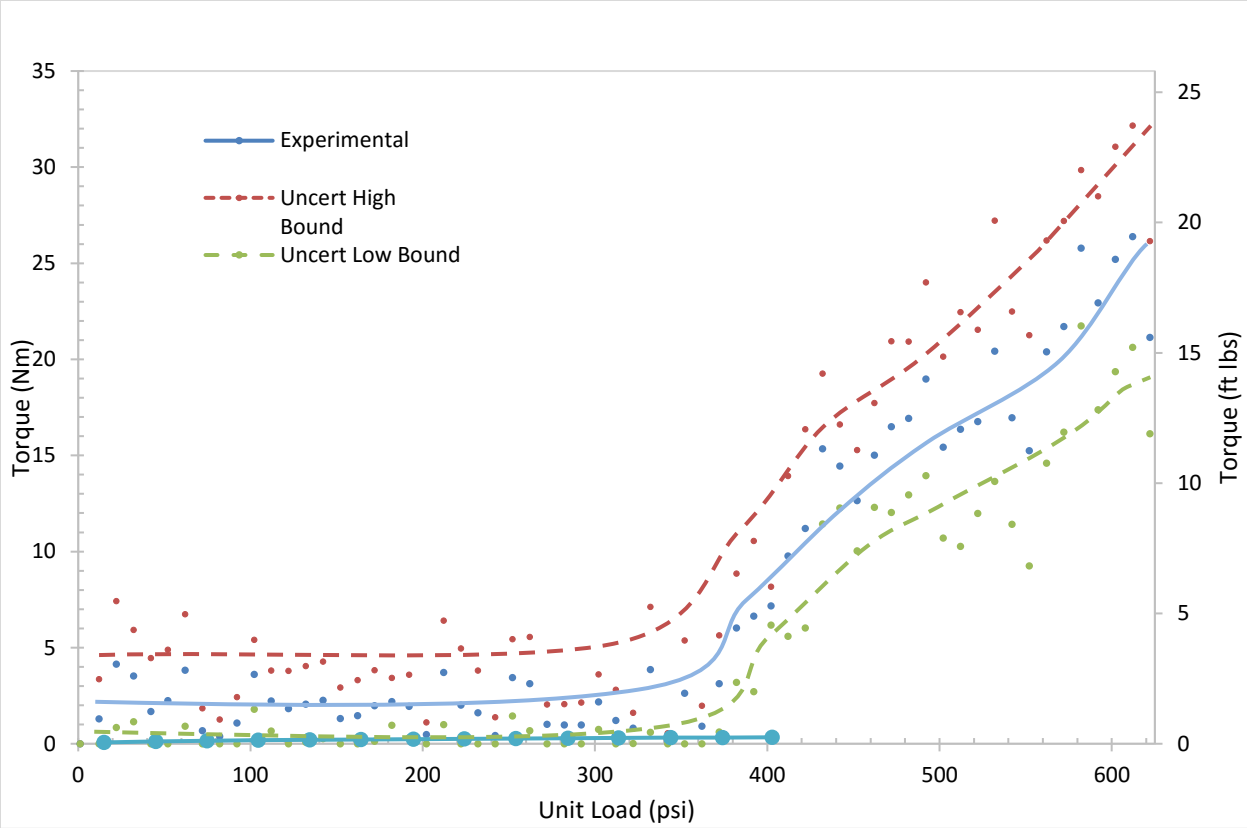

Figure 46 Torque vs unit load predictions vs experimental comparison

5.3 Experimental Results for PEEK

The same test matrix used for WC bearings was used for testing PEEK bearings as well. The PEEK can also withstand up to 350 psi (2.41 MPa) of unit load at 3600 RPM in full hydrodynamic lubrication. Figure 47 shows a picture of the PEEK pads after testing. The bearing operated in the hydrodynamic regime; however, there are signs of light wear. This is most likely due to intermittent contact with the runner from the film breaking since the film thickness for operating at 350 psi (2.41 MPa) is as low as 0.1 mils as discussed in 7.2. However, no significant contact occurred. If significant direct contact occurred, the bearing would most likely not have survived as PEEK is much softer than the WC coated runner and would be worn away rapidly as

seen in Figure 22 and Figure 25. The microscope images of the PEEK, shown in Figure 48, corroborates hydrodynamic lubrication operating regime with just slight amounts of wear.

Figure 47 PEEK bearing after operating at 350 psi (2.41 MPa) at 3600 RPM. Close up view on the right

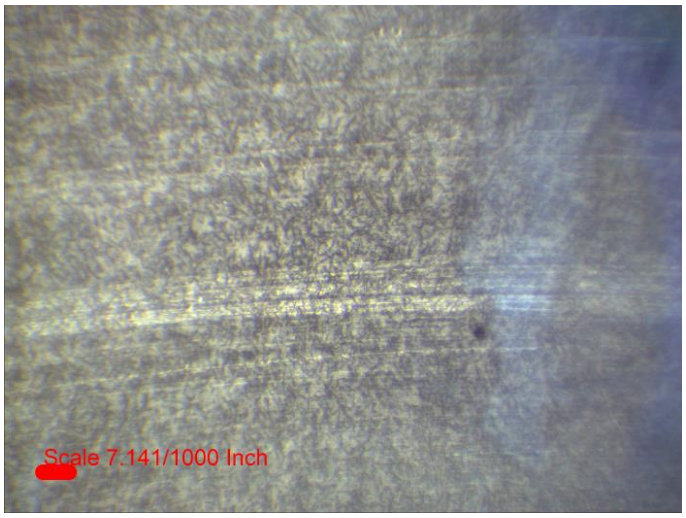

Figure 48 Microscope view of PEEK bearing after operating at 350 psi (2.41 MPa) at 3600 RPM

5.4 Wear Test Results

The wear test was conducted with the WC bearing at 3600 RPM and unit loads of approximately 365 psi or 2.41 MPa (i.e. above the hydrodynamic lubrication unit load capacity). Figure 49 and Figure 50 present the results. During the test, initial RTD temperatures skyrocketed to values approaching 200 C in the first few seconds. This indicates that the fluid film broke and rubbing has occurred, which means the bearing is operating outside of its hydrodynamic limit. Substantial wear occurred under this operating conditions. At the end of the first hour of testing, the RTDs were pulled away from the pad by the runner and were no longer in contact with the bearing pads. Thus, temperature readings after the 1 hour mark only measured the bulk water temperature, which explains the initial spike and subsequent steadiness of the temperature seen in Figure 50. The ambient water temperature experienced a steady rise due to the power dissipation induced by the rubbing despite the 20,000 Btu/hr (7.86 HP) heat exchanger in the fluid loop. At the end of the 3rd hour, water temperature approached 100C and was boiling in the reservoir.

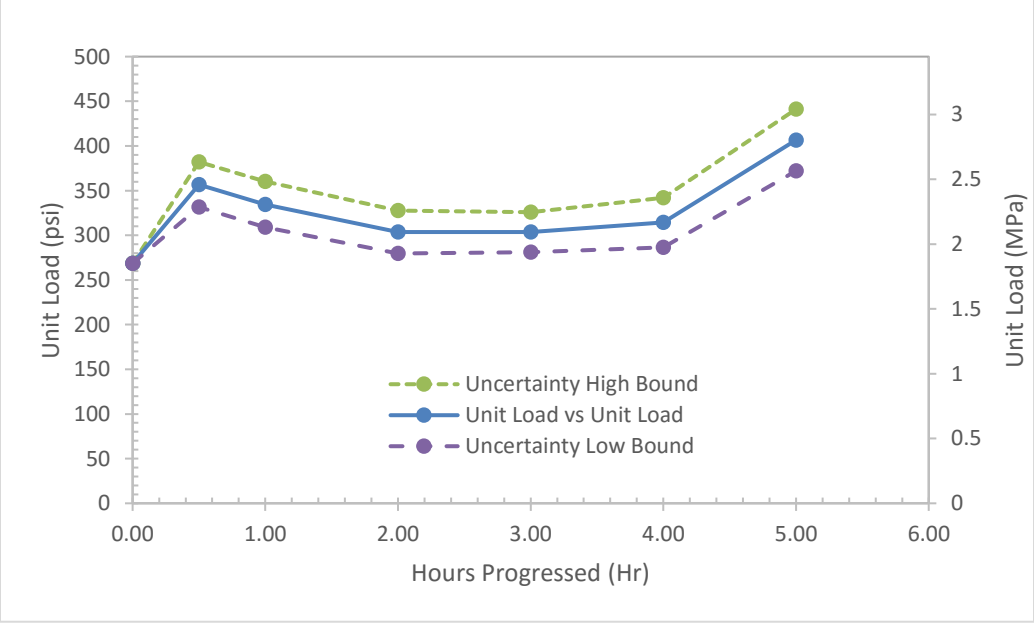

Figure 49 WC bearing unit load vs time for the 5 hr wear test

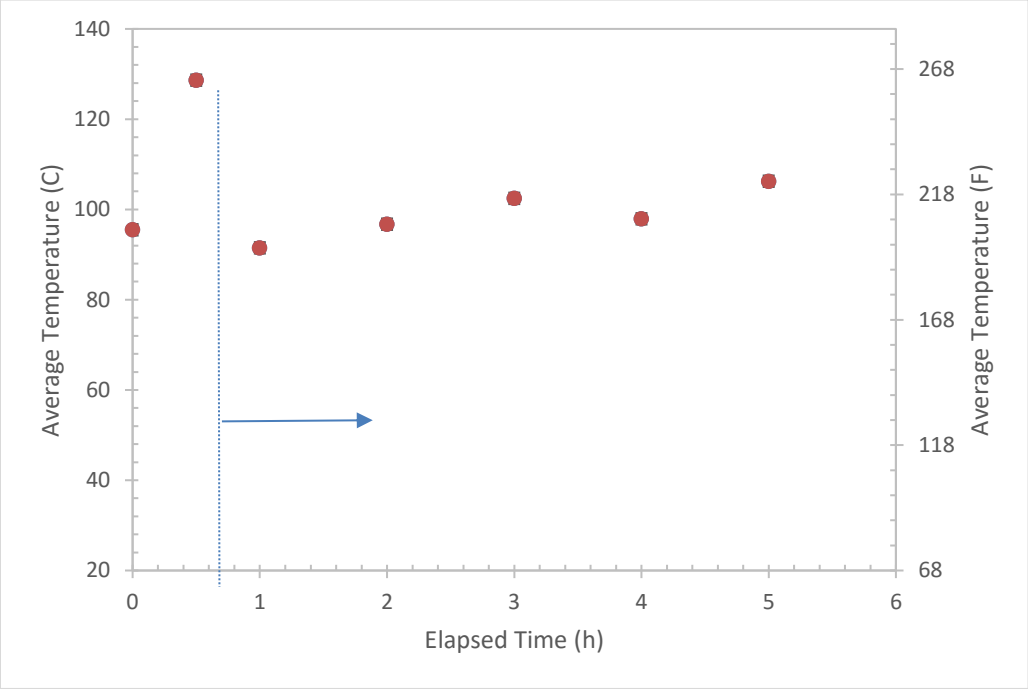

Figure 50 WC bearing average pad temperature vs time for the 5 hr wear test. The line and arrow indicate when the RTDs were likely flung out of the bearing

The bearing and runner experienced significant wear as seen in Figure 51. The WC wafer on the bearing pads displayed significant wear, chipping off in some instances. The runner exhibits the most severe wear as it is made with a comparatively softer 17-4 stainless steel with only a thin layer of WC coating. As the runner worn, it began to engulf the bearing which caused lubrication starvation and further intensified wear. The damage is severe enough to conclude that a boundary lubrication regime for this bearing is not a feasible economic solution.

Figure 51 WC bearing (left) and runner (right) after the wear test

6. CONCLUSION AND RECOMMENDATIONS

This thesis outlines the steps to model, machine, and commission a component level test rig to test process fluid lubricated thrust bearings. The test rig is capable of handling thrust bearings with diameters ranging from 4” to 8” (10 to 20 cm) at speeds of up to 3600 RPM (surface speeds of 16 m/s) with thrust loads of up to 60,000 lbs (266 kN). The vertically oriented test rig has provisions to test two bearings in tandem as well as test with a combination of water, air, and sand as the lubricating fluid. Furthermore, the test rig features a detachable bottom assembly enabling quick bearing changes and inspections. Initial testing in water lubrication yields the following conclusions:

Lubricant starvation can occur for water lubricated bearings in bath lubrication, which can cause destructive wear. Solutions to mitigate this include increasing the lubricant flow at the bearing and or pressurizing the test chamber.

PEEK and WC lined bearings have similar load capacities in hydrodynamic lubrication; however, once contact occurs, the softer PEEK polymer wears away quickly while the WC bearing can still operate in mixed lubrication due to its hardness.

Operating the WC bearing in contact lubrication yields destructive wear and temperatures as high as 200 C and thus is not recommended for continuous operation.

Film thickness in water lubrication is on the order of 0.1-0.3 mils. Thus, surface roughness and alignment become critically important as the film can easily break when external factors bridge this distance.

Recommendations for the future development of the rig are the following:

Sand and or air in the fluid loop may be flung to the outside or inside by centrifugal force during operation. An internal pipe that delivers fluid directly to the bearing is recommended when testing with sand and air so the ideal GVF and sand concentration test scenario can be maintained.

Testing in tandem will require the design of a load distributing plate that can split the load between bearings evenly. A plate like this should have a flexible pivot element that can tolerate small axial misalignments.

A more stable mounting mechanism for the thrust runner can yield more stable static proximity probe readings. Options include a new keyway design or grips attached to the rotor that hold the runner.

Though the slave bearing chamber is isolated from the test chamber, lubricating fluid does escape into the slave bearing chamber. This can cause rust in the slave bearings over time and distort baseline torque measurements. One solution is to replace the slave bearings with ceramic bearings which are much more resistant to lubricant contamination.

A motor with more horsepower and torque as well as a higher limit torque limiter coupling would allow testing bearings to failure. The higher torque limiter coupling also allows testing of contact bearings like polycrystalline bearings.

7. REFERENCES

[1] Rick von Flatern, 2015, "The Defining Series: Electrical Submersible Pumps." *Oilfield Review, Schlumberger.*

[2] "Electrical Submersible Pumps," last modified 2013, *Petrowiki.org*. Web.

[3] Durham, M., Williams, J., Goldman, D., 1990, "Effect of Vibration on Electrical Submersible Pump Failures," *SPE J Petroleum Technology,* **42** (2), pp. 186-190.

[4] Takacs, G., 2009, "Electrical Submersible Pump Manual," pp. 1-355.

[5] Harika, E., Bouyer, J., Fillon, M., Helene, M., 2013, "Measurements of Lubrication Characteristics of a Tilting Pad Thrust Bearing Disturbed by a Water Contaminated Lubricant," *Proceedings of the Institution of Mechanical Engineers Part J,* **227** (1), pp. 16-25.

[6] Harika, E., Bouyer, J., Fillon, M., Helene, M., 2013, "Effects of Water Contamination of Lubricants on Hydrodynamic Lubrication: Rheological and Thermal Modeling," *J Tribol,* **135** (4).

[7] Zhang, X., Wang, X., Li, X., Chu, X., 2012, "Study on Influence Factors of Bearing Capacity of Water-Lubricated Thrust Bearing and its Improving Methods," *Advanced Materials Research*, Xiamen, China, March 27-29th, 2012, pp. 949-952.

[8] Liu, Z., Wu, Z., 2010, "Numerical Calculation Analysis of Structural Parameters of Water Lubricated Thrust Bearing," *International Conference on Frontiers of Manufacturing and Design Science,* Chongqing, China, December 11-12th, 2010, pp. 1666-1671.

[9] Inoue, K., Deguchi, K., Okude, K., Fujimoto, R., 2012, "Development of the Water-Lubricated Thrust Bearing of the Hydraulic Turbine Generator," *IOP Conference Series: Earth and Environmental Science*, Beijing, China, August 19-23rd, 2012.

[10] Deng, X., Branagan, M., Weaver, B., Wood, H., 2017, "Thermal, Elastic, and Inertia Effects in Water-Lubricated Tilting Pad Thrust Bearings in the High-Turbulence Operating Region," *72nd Annual Meeting and Exhibition of the Society of Tribologists and Lubrication Engineers*, Atlanta, GA, May 21-25, 2017.

[11] Abramovitz, S., 1954, "Turbulence in Tilting-Pad Thrust Bearing," *American Society of Mechanical Engineers,* October 18-20th, 1954, pp. 1-8.

[12] Hu, N., Wu, N., Wang, S., Jiang, H., Li, Z., 2017, "Tribological Properties of Friction Pairs in Lubricant Contaminated with Particles under High Temperature," *Tribology Transactions,* **60** (4), pp. 663-669.

[13] Nie, Z., Li, G., Wang, X., Jiao, Y., Hua, Z., Yu, G., 2016, "Dynamic Experimental Research of PTFE-Faced Pad Thrust Bearings," *Tribology Letters,* **62** (1), pp. 1-8.

[14] Mahieux, C.A., 2005, "Experimental Characterization of the Influence of Coating Materials on the Hydrodynamic Behavior of Thrust Bearings: A Comparison of Babbitt, PTFE, and PFA," *J Tribol,* **127** (3), pp. 568-574.

[15] Wodtke, M., Wasilczuk, M., 2016, "Evaluation of Apparent Young's Modulus of the Composite Polymer Layers used as Sliding Surfaces in Hydrodynamic Thrust Bearings," *Tribol International*, **97** (5), pp. 244-252.

[16] Dieter, H., Thomas, F., Lorenz, S., 2015, "Qualification and Optimization of Solid Polymer Tilting Pad Bearings for Subsea Pump Applications," *Turbomachinery & Pump Symposia 2015,* Houston, Texas, Sept 14-17, 2015, pp: 112-117.

[17] Sexton, T. and Cooley, C., 2009, "Polycrystalline Diamond Thrust Bearings for Down-hole Oil and Gas Drilling Tools," *Wear* **267** (5-8), pp. 1041-1045.

[18] Knuteson, C.W., Sexton, T.N., Cooley, C.H., 2011, "Wear in Behavior of Polycrystalline Diamond Thrust Bearings," *Wear,* **271** (9-10), pp. 2106-2110.

[19] Sexton, T., Knuteson, C., Cooley, C., 2011, "Process Fluid Lubricated Polycrystalline Diamond Bearings for Applications in Marine Hydrokinetic Machines," *Tech. Proc. NSTI Nanotechnology Conf. Expo, NSTI-Nanotech*, Boston, MA, June 13–16th, pp. 695-698.

[20] Russell, C.I., 2011, "Hydrodynamic Thrust Bearings for Downhole Mud Motor Use," *AADE National Technical Conference and Exhibition,* American Association of Drilling Engineers, Houston, TX, 2011.

[21] Wang, X., 2005, "Running-in Effect on the Load Carrying Capacity of a Water Lubricated SiC Thrust Bearing," *Proceedings of the Institution of Mechanical Engineer,* **219** (2), pp. 117-124.

[22] Liang, X., Liu, Z., Yuan, C., Ouyang, W., Yan, X., 2016, "Design and Performance Analysis of a Water Lubricated Tilting Pad Thrust Bearing," *Proceedings of the International Offshore and Polar Engineering Conference*. Rhodes, Greece, June 26 – July 1st, 2016, pp. 908-913.

[23] Pasanen, A., Kleemola, J., Lehtovaara, A., 2008, "Development of a Test Device for the Evaluation of Hydrodynamic Lubrication in Thrust Bearings," *Tribologia,* **37** (4), pp. 12-20.

[24] Gregory, R.S., 1974, "Performance of Thrust Bearings at High Operating Speeds." *J Lubrication,* **96** (1), pp. 7-13.

[24] Bell, S., 1999, "Combining uncertainties from one unit of measurement to another," Measurement Good Practice Guide, National Physical Laboratory, Teddington, Middlesex, United Kingdom, pp. 14-15.

APPENDIX A

UNCERTAINTY ANALYSIS

There are several potential sources of error in the experimental setup. The uncertainty intrinsic to the instrumentation used is shown in Table 3. The RTDs used have extremely small error (± 0.5%). The hydraulic cylinders apply point loads individually; however, the pressure transmitted to them is split among a manifold that could distribute the pressure unevenly. Thus, a slight tilt could have formed in the test bearing, but this tilt could be captured by the load cells. Unfortunately, one load cell broke during testing so most of the data was obtained with only two operational load cells.

Uncertainty Chart	**Range (US Units)**	**Range (SI Units)**	**Uncertainty Over Full Range**
Load Cells	0-10,000 lbs	0-44.48 kN	± 0.5% Nonlinear when under 50 lbs
Torquemeter	0-36.8 ft-lb	0-50 Nm	± 0.1%
Water Flowmeter	0-20 GPM	0-7.57e-2 m^3/minute	± 1.5%
Pressure Transducer	0-500 psi	0-3.447 MPa	± 0.08%
Proximity Probes	10-40 mils	254-101.6 microns	± 2.5%

Table 3 Uncertainty in instrumentation setup

The combined standard uncertainty for the torque is calculated by summing the squares of the standard uncertainty of each source of error [24]. The torque is calculated as follows:

$$Torque = Input\ Voltage * Conversion\ Factor \qquad \text{(A-1)}$$

Because the torque is calculated from a simple function, the summation in quadrature for the u(Torque) or the uncertainty of torque is as follows:

$$\frac{u(Torque)}{Torque} = \sqrt{\left(\frac{u(Inp.Volt)}{Inp.Volt}\right)^2 + \left(\frac{u(Data\ Acq.)}{Data\ Acq.}\right)^2 + \left(\frac{Stand.Dev.of\ Torque}{Torque}\right)^2} \qquad \text{(A-2)}$$

Each term in the summation is a non-dimensionalized error percentage parameter that is propagated to the end result. The first two terms in the A-2 are the accuracy error garnered from the data acquisition while the third term is the error from the variability in sampling data. Likewise, the error derived in the temperature and proximity probe readings follows a similar format as they are all simple multiplicative functions. They are shown below in A-3 and A-4.

$$\frac{u(Temp)}{Temp} = \sqrt{\left(\frac{u(Inp.Resistance)}{Inp.Resistance}\right)^2 + \left(\frac{u(Data\ Acq.)}{Data\ Acq.}\right)^2 + \left(\frac{Stand.Dev.of\ Temp}{Temp}\right)^2} \qquad \text{(A-3)}$$

$$\frac{u(Prox\ Probe)}{Prox\ Probe} = \sqrt{\left(\frac{u(Inp.Volt)}{Inp.Volt}\right)^2 + \left(\frac{u(Data\ Acq.)}{Data\ Acq.}\right)^2 + \left(\frac{Stand.Dev.of\ Prox\ Probe}{Prox\ Probe}\right)^2} \qquad \text{(A-4)}$$

APPENDIX B

MACHINE DRAWINGS

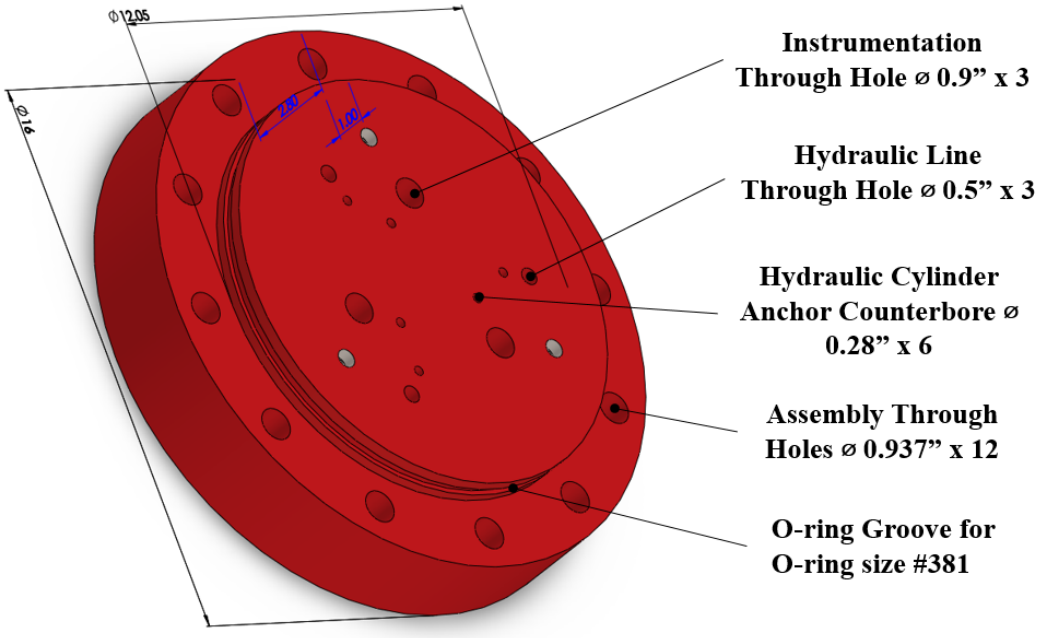

Figure 52 End flange model and notable features

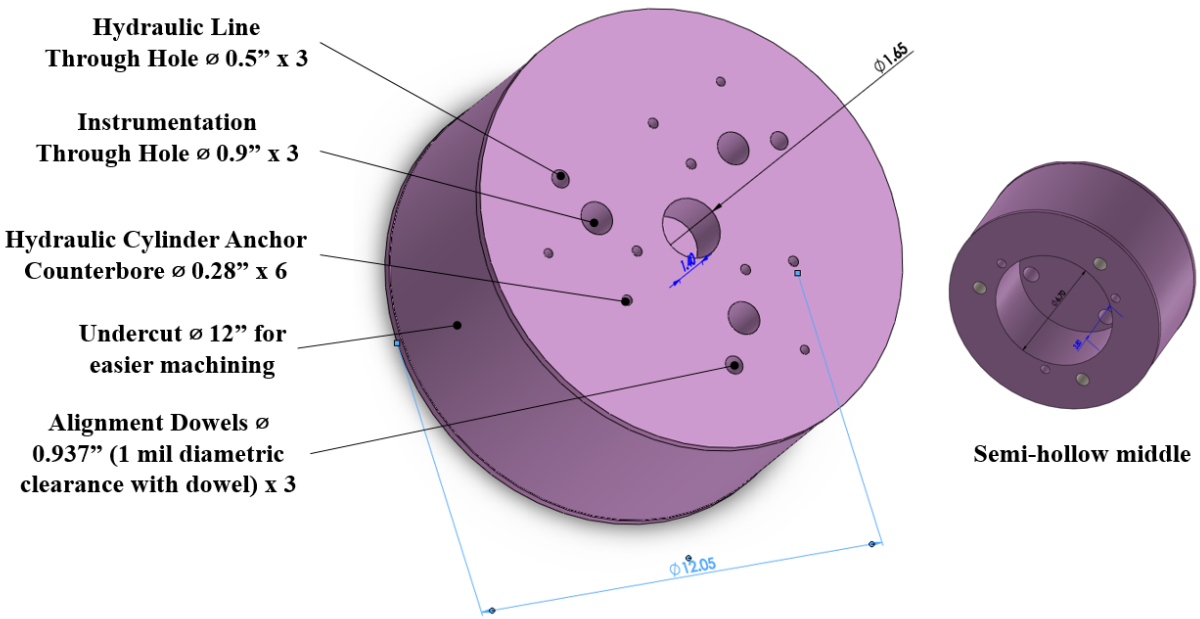

Figure 53 Spacer model and notable features

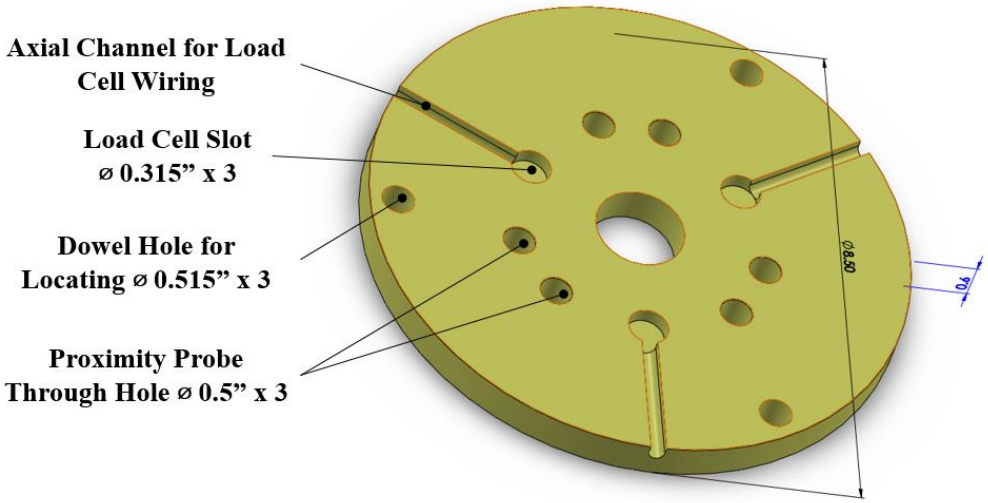

Figure 54 Load cell plate model and notable features

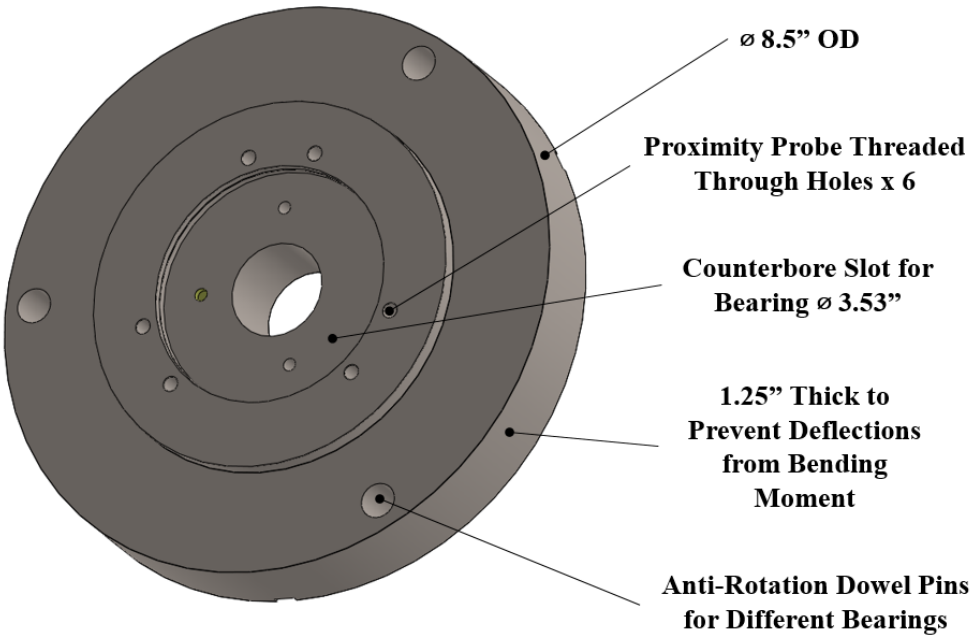

Figure 55 Bearing plate model and notable features

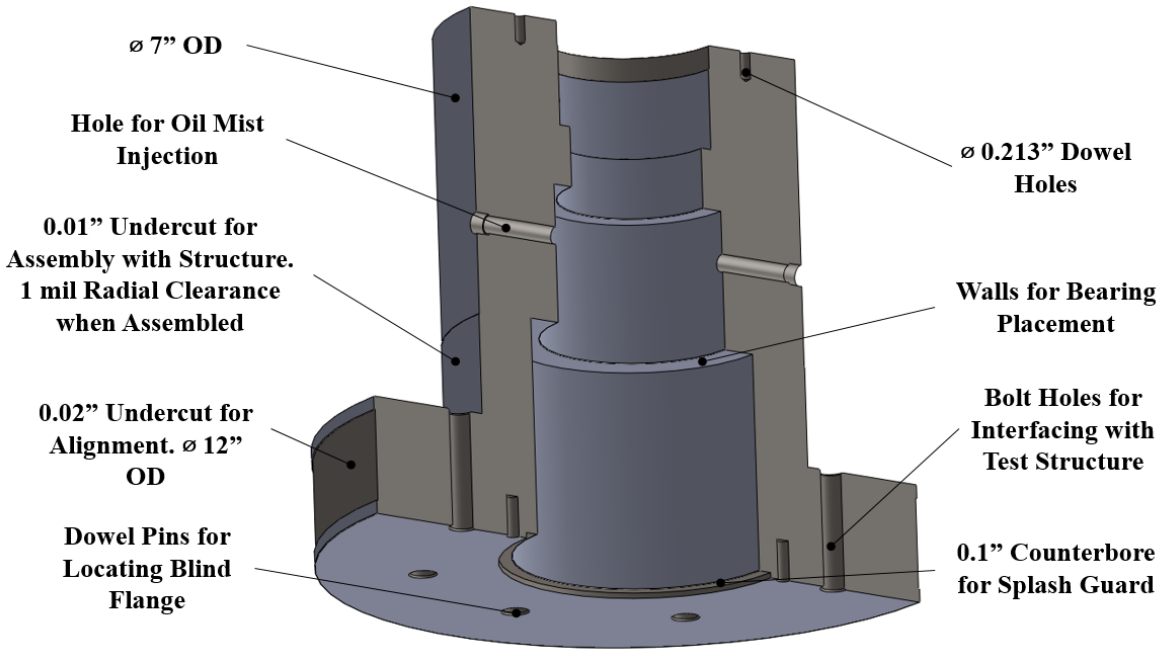

Figure 56 Slave bearing casing model and notable features

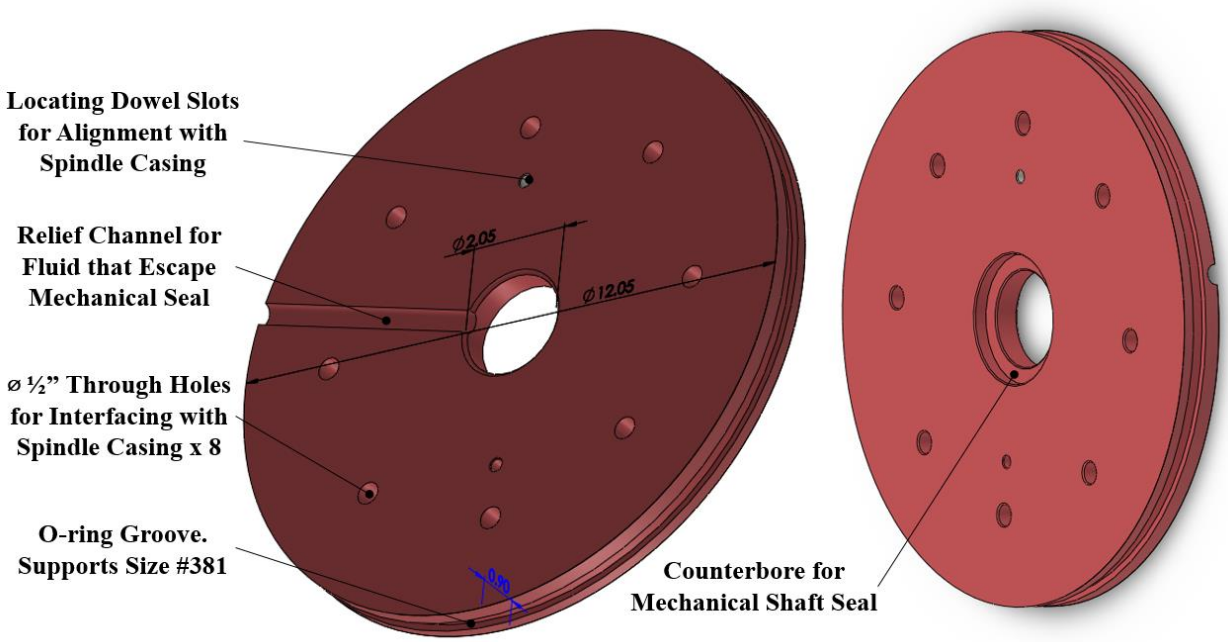

Figure 57 Isolating blind flange model and notable features

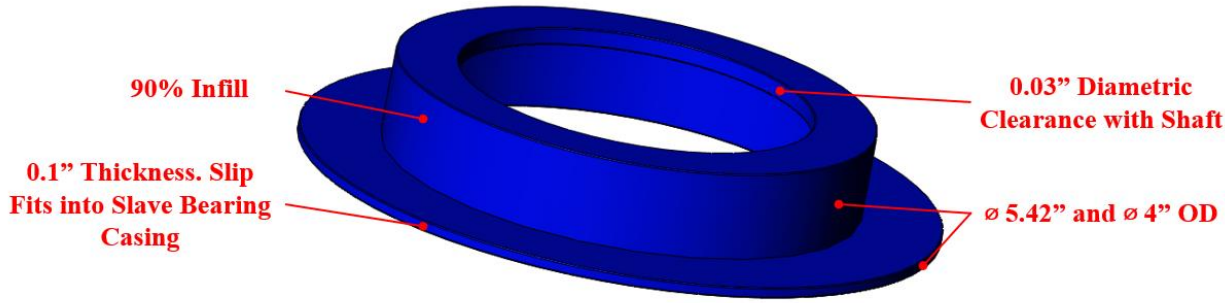

Figure 58 Plastic splash guard model and notable features